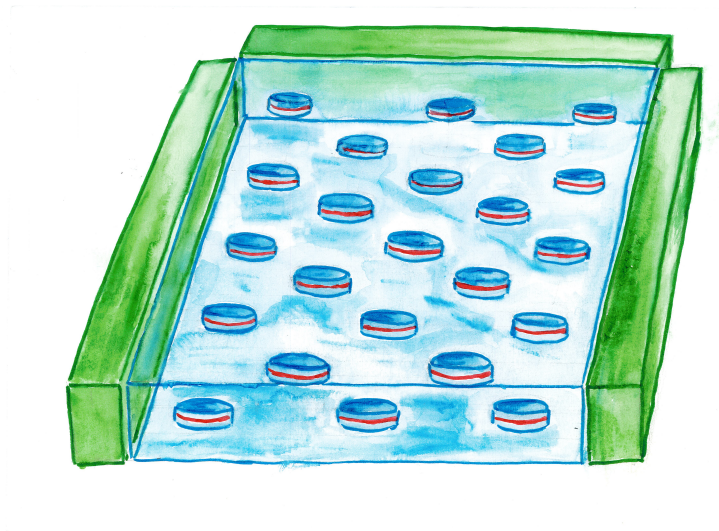UNIVERSITY OF AMSTERDAM

SCIENCE FOR ENERGY AND SUSTAINABILITY

MASTER THESIS

Directing Quantum Dot Emission in LSCs

Author:
Kyra ORBONS

Supervisor:
Tom VEEKEN
Examiner:
Prof. Dr. Albert POLMAN
Second Examiner:
Dr. Katerina
DOHNALOVA-NEWELL

August 6, 2019

"We stand now where two roads diverge. But unlike the roads in Robert Frost's famous poem, they are not equally fair. The road we have long been travelling is deceptively easy, a smooth superhighway on which we progress with great speed, but at its end lies disaster. The other fork of the road —the one 'less traveled by'— offers our last, our only chance to reach a destination that assures the preservation of our earth."

Rachel Carson, *Silent Spring*

Abstract

Kyra ORBONS

Directing Quantum Dot Emission in LSCs

Luminescent solar concentrators (LSCs) provide potential for new photovoltaic implementations. However, they are hampered by low efficiencies. This is in part attributed to their semi-transparency, but also due to several other loss mechanisms. A major loss in all LSCs is light escaping from the waveguide through the escape cone. In this work, we present a novel way to reduce this loss. By embedding quantum dots in high index dielectric nanostructures, their emission pattern can be altered such that the emitted light is mostly directed below the critical angle for total internal reflection of a waveguide in air. We use FDTD simulations to determine the optimal geometry of these structures, that are made out of TiO_2. This is followed by the experimental realization of these structures with the quantum dots inside. We demonstrate that the photoluminescence is preserved during the fabrication process. Finally, we provide preliminary cathodoluminescence measurements that give the first indication of directive emission. Further research could clarify the modes that cause the directive behavior of the particles. Moreover, the next fabrication steps are to embed the nanostructures in a waveguide and finally connect this to spectrally matched solar cells.

Contents

1 Introduction

123 years ago the first paper that quantified the effect of greenhouse gases on the earth's temperature was published, projecting an increase of 4-6 degrees Celsius of the global average temperature if CO_2 concentrations were to double [3]. At the time, scientists were aware that such a doubling was a theoretical possibility due to the burning of fossil fuels over a long period. At the end of the 1950s, regular measurements of atmospheric carbon dioxide were started by Charles David Keeling at Mauna Lao Observatory. Already a few years later he was able to conclude that CO_2 concentrations were rising steadily [34]. The continuation of this trend is dramatically visible in figure 1.1, which is now known as the *Keeling curve*. Since then it has become ever more clear that the human greenhouse gas emissions and deforestation are to blame for the increase of atmospheric carbon dioxide and the resultant temperature increase of, as of yet, approximately 1.1° C compared to pre-industrial levels [28]. Furthermore, scientists are increasingly aware of the dire consequences of global warming for the Earth's ecosystem and humanity [36].
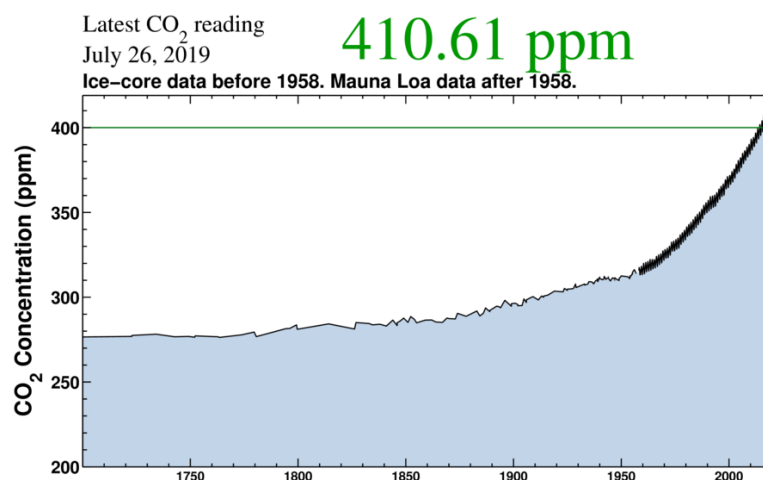

FIGURE 1.1: The Keeling Curve from 1700 till now by the Scripps Institution of Oceanography [39].

Hence scientists' warnings have grown in quantity and urgency for the past decades. However, our pollution is ever-growing, putting increasing pressure on the planet's ecology and her resources. Although support for measures cutting down on emissions of greenhouse gasses is growing, humanity still emits more CO_2 each year than ever before. The reality we face now is that the effects of climate change are starting to penetrate our everyday lives. Extreme weather events are increasing both in intensity and frequency. Food and water scarcity as a result of droughts are

already causing major problems, particularly in the Global South. Moreover, numerous latent effects of current emissions will only become apparent in a couple of decades or centuries.

The International Panel on Climate Change's report in 2018 had a very clear message: urgent an unprecedented action is needed to prevent extreme and irreversible damage to our ecosystems [2]. This means that scientists and policymakers alike need to join forces to facilitate the transformation of our energy system in order to keep global warming below 2° C, and ideally below 1.5° C. Even though neither of these targets can be considered safe [25, 36], it is still much better than our current track: towards 3-5°C of warming by the end of this century, with disastrous consequences for our species. The coming years are essential in making sure this does not happen. The sooner we phase out fossil fuels, the higher the chance of sustaining a planet with a habitable climate for all life on earth.

To do this we will certainly need to alter our consumption patterns in the Global North. The only countries that are currently following the Paris climate agreement in terms of their emissions are the Philippines, Ethiopia, India, Costa Rica, and Bhutan. While only Morocco and Gambia are on track with the 1.5°C target [40]. These are not necessarily the countries that are at the forefront of renewable technology. However, our society relies heavily on energy consumption and this is not bound to change in the (near) future. Along with reduction and reforestation, an enormous capacity of renewable resources will thus have to be installed.

The most prominently available source of energy is shining right onto to us; the sun. In 2000 the United Nations Development Programme's World Energy Assessment estimated the annual potential of solar energy to be 1,575–49,837 exajoules [13]. This potential can be actualized by photovoltaics (PV). Photovoltaic devices are becoming more and more cost-effective and are currently the largest source of renewable energy in civil and industrial buildings [14]. However, fitting them in the urban environment proves a difficult task, and is largely lagging for aesthetic reasons. People generally dislike the look of the typical dark blue solar panel. Developing photovoltaic devices that are less obtrusive could offer a solution to this problem. Scientists are increasingly conscious of this, and the focus is no longer just on efficiency, durability, and cost reduction, but also on the aesthetics of the solar panel.

Luminescent solar concentrators (LSCs) open up new possibilities in this field. They come in a variety of shapes and colors and enable the production of new devices such as semi-transparent PV windows. By replacing existing energy-passive glazing with these new panels, buildings could be transformed into energy generating systems, without significantly altering their appearance, see figure 1.2 for an example. This seamless integration could lead to increased social acceptance, making it more likely that they will be implemented on a large scale. Moreover, since production costs of LSCs are typically lower than those of traditional silicon PVs, it allows for further cost reductions [42].

Despite all of these benefits, LSCs have not yet been commercialized, in part because of the low efficiencies that have been realized [14, 30]. Research efforts are directed towards the reduction of the loss mechanisms that contribute to these poor results. These include the use of selective mirrors and novel luminophores.

The introduction of new types of luminophores, such as highly emissive perovskites, nanocluster phosphors, and colloidal quantum dots (QDs), has recently led to a revival of research on LSCs [42]. These novel emitters have largely replaced the use of organic dye molecules that suffered from limited spectral coverage, low

photoluminescence, and strong losses due to reabsorption [42]. Semiconductor QDs can be produced at a low cost, without the use of heavy metals.

This thesis presents a novel approach to reduce escape cone losses in LSCs. By employing high-index dielectric nanoparticles, luminophore emission is directed into the waveguided modes while simultaneously enhancing absorption. We determine the ideal geometry of such resonators through simulations. The main focus of this research is then the experimental realization of these structures.

The thesis is structured as follows. We first discuss the working mechanism of LSCs, including the various losses in 2.1. We then briefly look at the achieved efficiencies for these devices in 2.2 followed by the current research that aims to enhance these efficiencies (2.3) where we shortly introduce our approach. Chapter 3 is then dedicated to dielectric resonant nanostructures. We first provide some theoretical background on the behavior of these particles in 3.1, after which we proceed with the numerical simulations that we use to optimize the geometry of TiO_2 resonators that should enhance absorption and direct emission of quantum dots in LSCs (3.2). The fabrication methods of the presented design are then treated in chapter 4. Photoluminescence and preliminary cathodoluminescence measurements are consecutively executed on the finalized samples. The results of these measurements are presented in chapter 5. These are followed by a discussion of the limitations of this research and potential next steps, see 6. We conclude with an overview of the current achievements and an outlook on future research.
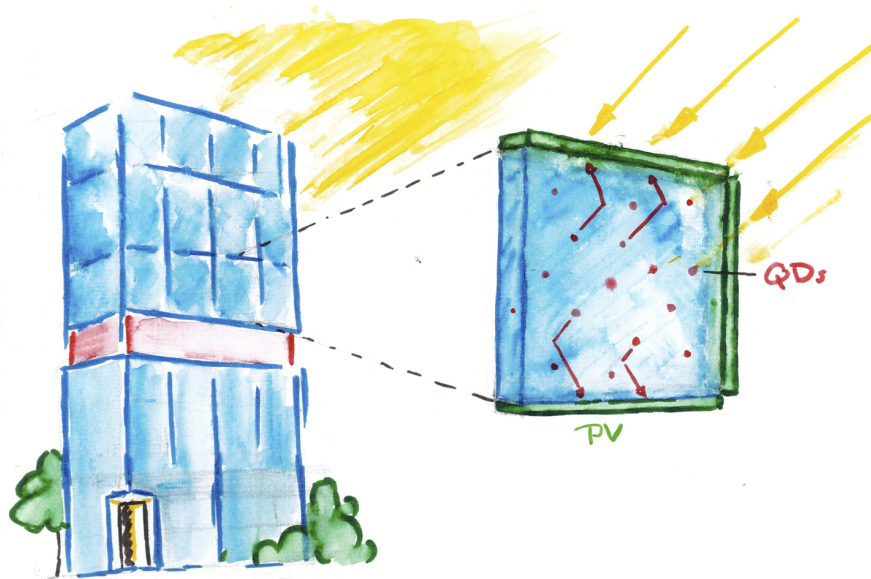

FIGURE 1.2: An example of LSC intergration in architecture.

2 Luminescent Solar Concentrators

A luminescent solar concentrator (LSC) is a transparent device that traps part of the incident light and redirects (concentrates) that light towards its edges. This concentrated light can be converted to electricity by combining the LSC with spectrally matched photovoltaics (PV). On their own, they are a semitransparent pane and can hence function as an energy-generating window when connected to PV. Alternatively, the LSC can be embedded in a tandem structure together with a regular solar cell to increase overall efficiencies. LSCs have interesting use cases and theoretically a lot of potentials. Unfortunately, the device efficiencies are as of yet too low to effectively implement them in the real world.

This chapter is based on an earlier literature review [33][1]. In the first section, we explain the basic working mechanism of an LSC and the multiple loss mechanisms that are inherent to LSCs. In the next section, we discuss the efficiencies that have been achieved so far. Finally, we look at some of the explored pathways to mitigate the (most prominent) losses, including our approach.

2.1 Working Mechanism

An LSC consists of a transparent slab in which highly emissive luminophores are embedded. The slab functions as a waveguide for the light emitted by the luminophores. In brief, the system works as follows. Light penetrates the top surface of the waveguide and is then absorbed by the luminescent molecules. These molecules are either embedded in the waveguide, applied in a separate layer on the top or bottom of the slab, or contained in a liquid solution that is sandwiched between two glass plates. The absorbed light is then re-emitted at a longer wavelength, part of which gets trapped in the waveguide by total internal reflection. This light is then concentrated on the edges of the slab where it can be collected and converted to electricity by PV. The slab generally consists of a polymer, such as PMMA or PLMA. The luminophores come in the form of organic dyes, organo-metallic particles, and quantum dots (QDs), each of which has distinct limitations and advantages. A schematic representation of the working principle of an LSC is shown in figure 2.1.

Total internal reflection inside a waveguide surrounded by air occurs at angles above the critical angle, θ_c which is given by Snell's law:

$$\theta_c = \sin^{-1}\left(\frac{1}{n}\right) \tag{2.1}$$

with n the refractive index of the waveguide. For waveguides, this value is typically close to 1.5. Most photons that are emitted within the escape cone, i.e. below the critical angle, are lost through the surface. This is a major part of the losses in every type of LSC. There are also multiple other loss mechanisms, which are illustrated in

---

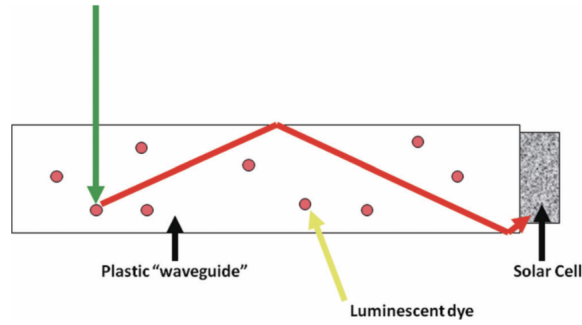[1]This is a brief overview, for an elaborate explanation see [14].

FIGURE 2.1: A simple graphical presentation of the main working mechanism of an LSC, taken from [14].

figure 2.2. The overall optical efficiency of the LSC is given by the following equation

$$\eta_{opt} = (1 - R)P_{TIR} \cdot \eta_{abs} \cdot \eta_{PLQY} \cdot \eta_{Stokes} \cdot \eta_{host} \cdot \eta_{TIR} \cdot \eta_{self}. \tag{2.2}$$

Here R is the reflection of solar light from the waveguide surface, P_{TIR} is the total internal reflection efficiency, η_{abs} is the fraction of solar light absorbed by the luminophores, η_{PLQY} the photoluminescence quantum yield of the luminophores, η_{Stokes} is the energy lost due to the heat generated during the absorption and emission event, η_{host} is the transport efficiency of the waveguided photons through the waveguide, η_{TIR} is the reflection efficiency of the waveguide determined by the smoothness of the waveguide surface and finally η_{self} is the transport efficiency of the waveguided photons related to reabsorption of the emitted photons by another luminophore [14]. These loss mechanisms have so far resulted in rather low efficiencies. Research in the field has recently seen a revival and aims to find solutions to minimize losses [14, 30]. We will now discuss each in more detail.
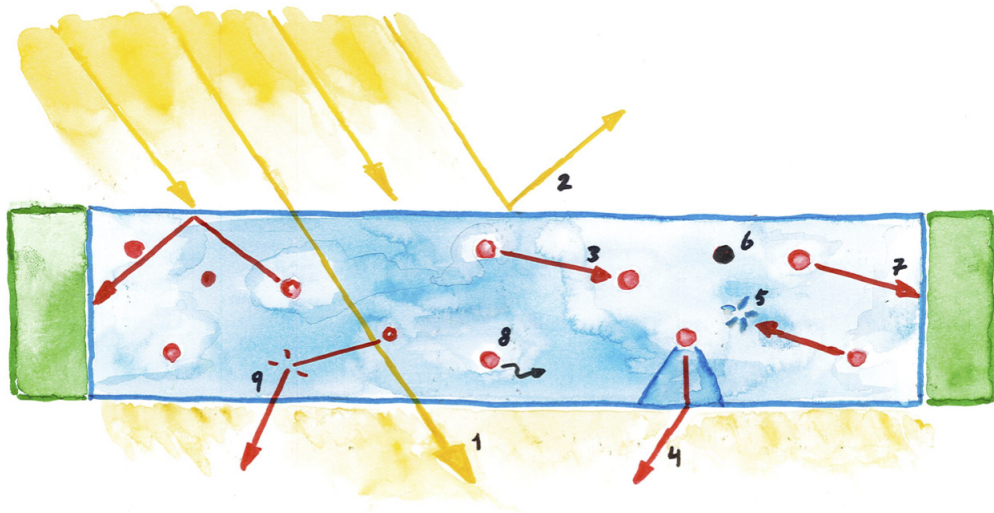

FIGURE 2.2: An overview of various loss mechanisms: 1) represents light that is not absorbed by a luminophore, 2) reflection at the surface, 3) reabsorption, 4) escape-cone loss, 5) parasitic absorption by the waveguide 6) unstable luminophores, 7) losses in the solar cell, 8) limited photoluminescence quantum efficiency, and 9) internal scattering. This figure is based on [14].

The first potential loss is caused by surface reflection (figure 2.2, 2). Photons that do not penetrate the top layer of the waveguide will not get absorbed within that waveguide and are thus lost. Once a photon enters the material it can either pass through without encountering a luminophore and leaving the bottom surface (figure 2.2, 1), or get absorbed by a particle. Whether this happens depends on the energy of the photon, the band structure of the luminophore, and the luminophore concentration. A higher concentration increases the probability of a photon encountering a luminophore. However, an increase in the luminophore concentration comes at the cost of the transparency of the LSC as this means that less light is passing through. A trade-off between efficiency and the implementation as a transparent solar device has to be considered for individual designs.

Given that we know the desired transparency of the design, it is necessary to minimize losses across the board. Once a photon passes through the waveguide and is absorbed by a luminophore, the first necessary steps have been taken towards the final goal of conversion to electric energy. Still, many options for losses remain. Some photons will not be re-emitted due to a limited photoluminescence quantum yield (PLQY) (figure 2.2, 8), the energy is then lost as heat and vibration. (figure 2.2, 8) represents the escape cone loss that we have already mentioned. Various methods have been put forth to prevent this from happening, see section 2.3. This loss mechanism is the focus of this thesis. We discuss its minimisation in sections 2.3 and 3.2.
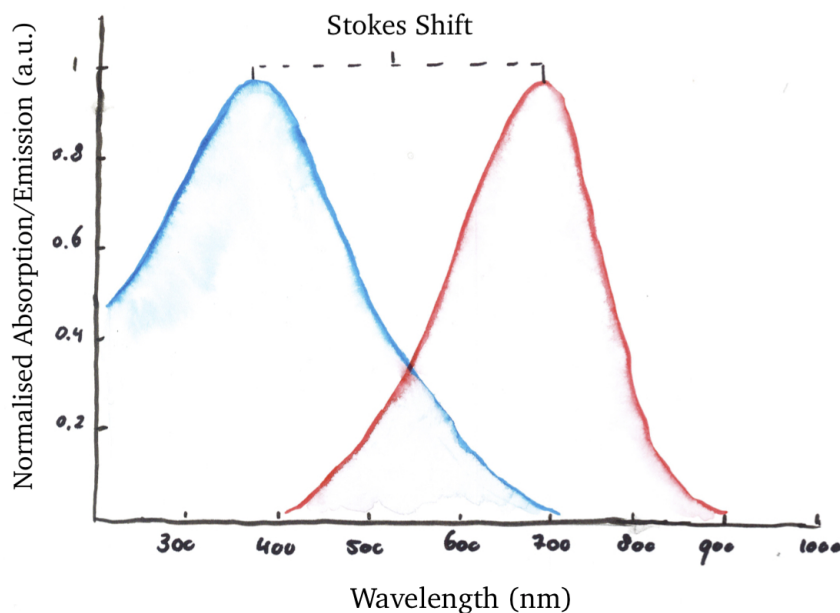

FIGURE 2.3: A schematic representation of the absorption (blue) and emission (red) spectra of a luminophore, the distance between the peaks of the absorption and emission spectra indicates the Stokes shift.

The Stokes shift indicates the amount of energy that is lost due to the difference in wavelength, and thus energy, between the absorbed and subsequently emitted photon, as shown in figure 2.3. By definition, the peak absorption wavelength is shorter than the peak emission wavelength, implying an inherent energy loss. However, that does not directly mean that the Stokes shift must be minimized. A bigger Stokes shift will prevent reabsorption (figure 2.2, 3) of the emitted photons because of the smaller overlap between absorption and emission wavelengths. The wavelength of

the emitted photons ideally peaks at the smallest possible wavelength where the absorption is minimal such that the overlap between optical absorption and emission spectra is minimized. An even larger Stokes shift would result in a higher energy loss.

The heat generation associated with the energy loss changes the entropy of the system and thereby the maximum achievable ratio between incoming and emitted irradiance, called the concentration. The maximum concentration can be approximated by

$$C \approx \frac{e_2^3}{e_1^3} \exp \frac{e_1 - e_2}{kT_0}, \tag{2.3}$$

where e_1 and e_2 are the energies of the absorbed and emitted photons, respectively, k is the Boltzmann constant and T_0 the ambient temperature. A large Stokes shift thus implies a higher maximum concentration [14]. The concentration factor is generally not a limiting factor, unless the Stokes shift is rather small. Recent research on quantum dots opened up new opportunities for tuning the Stokes shift.

Most of the emitted photons will be transported to the edges of the waveguide, in particular when the Stokes shift is large. Although losses can still occur due to parasitic absorption (figure 2.2, 5) of the waveguide itself and imperfections of the surface (figure 2.2, 9) allowing photons to escape the LSC. Like reabsorption, these issues become increasingly significant when upscaling the area of the LSC. However, these losses can be efficiently suppressed by choosing the right matrix material for the type of luminophore that is used. The last loss is caused by the limited efficiency of the solar cells at the edges of the device (figure 2.2, 7). This loss is typically low, as highly efficient cells are generally used and can be matched with the emission spectra of the luminophores.
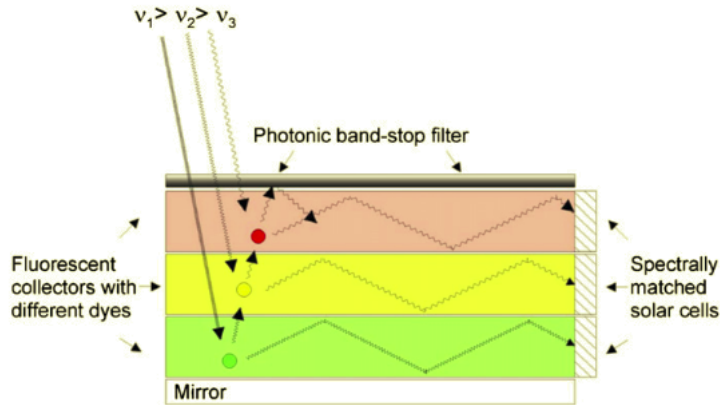

FIGURE 2.4: A tandem stack based on LSCs with different types of fluorescent dye molecules. This configuration allows for photon recycling, meaning that photons that are lost in one layer can be absorbed by the next. The different layers are attached to spectrally matched solar cells. This figure was taken from [20]

Other methods for increasing the overall efficiency of a device include tandem stacking [20, 42]. By employing multiple LSCs with different absorption properties it is possible to make more efficient use of the solar spectrum.

The working principle of these tandem cells is analogous to multijunction photovoltaics: (low energy) photons that are not absorbed by the top layer pass through to a second, or higher, layer and can subsequently be absorbed in that layer. These

various layers are connected to spectrally matched solar cells, as shown in figure 2.4. Tandem LSC systems typically achieve higher efficiencies at the cost of transparency and thus design flexibility.
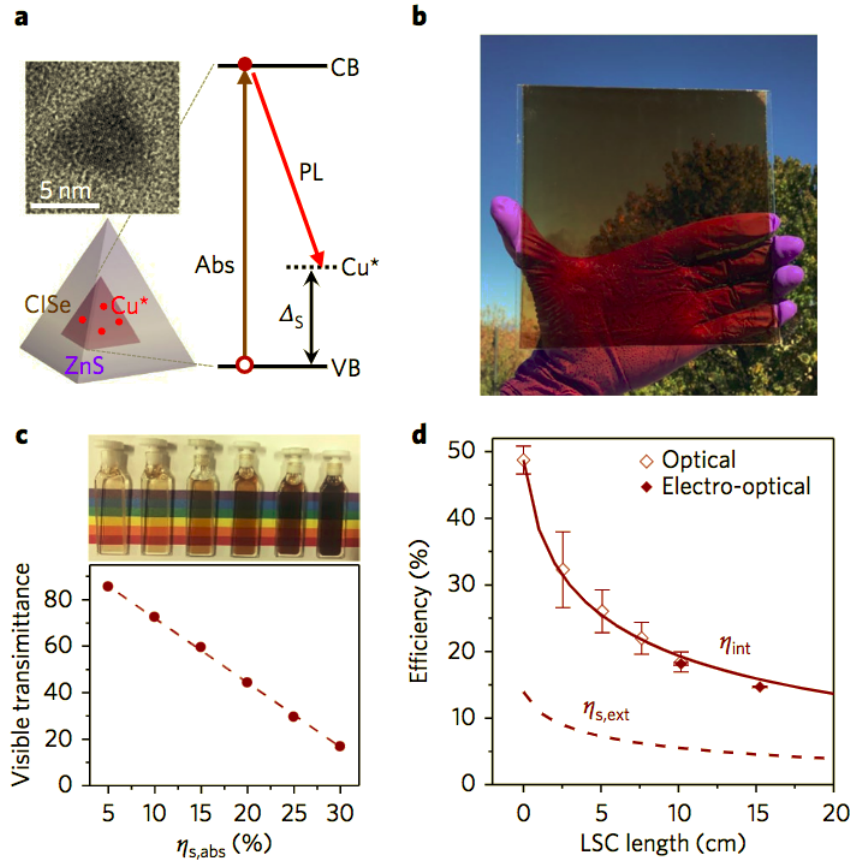

FIGURE 2.5: Characterisation of the bottom tandem-LSC layer based on CuInSe$_2$/ZnS QDs. (a) TEM image and schematic model of an individual CISe/ZnS QD, (b) 232cm^2 CISe-QD LSC, (c) Solution samples of CuInSe$_2$/ZnS QDs with different absorptances, these absorptances are plotted with the corresponding visible transmittance, that reflects the degree transparency, (d) Length dependent η_{int} (solid brown line) and external quantum efficiency (dashed line). Figure taken from [42].

High-performance semitransparent QD based tandem structures have already been realized [42]. Figure 2.5 shows an example of such a system with two types of QDs. The top layer consists of strongly luminescent Mn^{2+} doped Cd$_x$Zn$_{1-x}$S QDs, which absorb near-infrared. The bottom layer consists of CuInSe$_2$, which strongly absorbs wavelengths above 440 nm. The achieved power to electricity conversion efficiency (PCE) for this large area (15.24 × 15.24 cm^2) stack, coupled to GaAs solar cells, was 3.1%, but could be increased to 3.8% by using spectrally matched solar cells [42]. When transparency is not important in the design strategy fewer constraints are posed on the methods for loss reduction. Therefore, these set-ups are particularly suitable to use in combination with backreflectors and band-stop filters (see section 2.3).

2.2 Device Efficiencies

It is difficult to position LSCs in the PV field, in part because interpreting efficiency values gives rise to confusion [14]. Net efficiencies of LSC devices tell us little about the achievements of the waveguide itself, while merely reporting the efficiency of the waveguide can be misinterpreted as the PCE and leaves out the final energy conversion. Moreover, the surface area plays a much bigger role in the device performance than in conventional semiconductor PVs. Finally, device thickness will enhance the efficiency but, for semi-transparent LSCs, at the cost of transparency. A standardized method could potentially overcome issues concerning comparing various devices.

That being said, the current record PCE dates back to 2008 and is 7.1% for a dye-based LSC with a back reflector, connected to four GaAs solar cells. Figure 2.6 gives an overview of various LSC efficiencies that have been achieved so far. It remains to be seen what threshold efficiency value is needed to start producing them on a commercial scale. This will probably largely depend on additional qualities, such as production costs, design flexibility, and the political climate.

fluorophore	emission QY (%)	LSC size $L \times W$ (cm^2)	optical efficiency (%)	PCE (%)	solar abs* (%)
CuInS$_2$/ZnS QDs	91 (66% film)	10 × 10	8.1	2.94	35.5
CuInS$_2$/ZnS QDs	91 (66% film)	10 × 10	8.1	2.18	35.5
Lumogen F Red305		5 × 5		7.1	
Fluorescence Yellow CRS040					
CuInSe$_2$/ZnS QDs	72	15.2 × 15.2	6.4	3.1	24.0
Mn:Cd$_x$Zn$_{1-x}$S/ZnS QDs	78				4.6
CuInS$_2$/CdS QDs	75	7.5 × 7.5	5.7		
CuInSe$_2$/ZnS QDs	72	15.2 × 15.2	5.5	2.5	28.0
CuInSe$_x$S$_{2-x}$/ZnS QDs	40	12 × 12	3.3		10.0
Si QDs	50	12 × 12	2.9		
CdSe/CdS/CdZnS/ZnS QDs	45	4.95 × 3.1	na	2.8	31.0
CdSe/Cd$_{1-x}$Zn$_x$S QDs	70	10.2 × 10.2	1.9		6
CdSe/Cd$_x$Pb$_{1-x}$S QDs	40	7 × 1.5	1.4	1.15	
PbS/CdS QDs	40−50	2 × 1.5	6.1		
PbS/CdS QDs	40−50	10 × 1.5	1.1		
CdSe/CdS QDs	45	21.5 × 1.35	0.6		

FIGURE 2.6: Table with various achieved efficiencies to date, adapted from [4].

2.3 Current Research on LSCs

Recent breakthroughs in the design of quantum dots have caused a revival in the field of LSC research. While organo-metallic chromophores had limited spectral coverage and organic dyes showed a large overlap between emission and absorption spectra (small Stokes shift) [29, 30], colloidal quantum dots have a broad absorption spectrum and can be tuned to match the peak response of the solar cells attached to the waveguide. Moreover, their Stokes shift can be adjusted by doping, heterostructures, and ternary semiconductor compositions resulting in a negligible overlap between absorption and emission functions [30]. Suppression of reabsorption is of particular interest in large-area devices, as the probability of reabsorption increases with the distance the photons have to travel before reaching the edges of the waveguide.

Among semiconductor QDs are I-III-VI$_2$ type semiconductors, such as CuInS$_2$ and CuInSe$_2$, that are free of toxins and reduce reabsorption losses while extending the coverage of the solar spectrum [29, 42]. They typically have a high photoluminescence quantum yield which thus results in relatively high overall efficiencies. Unfortunately, selenium and indium are prone to issues concerning availability. The (weak) absorbance across a broad spectrum causes LSCs based on semiconductor QDs to be fairly colorless, making them suitable to use as semi-transparent windows [29]. This is demonstrated in figure 2.7. The absorption and emission spectrum of the QDs that were used in these LSCs is given in figure 2.8. The emission function of the QDs perfectly matches the EQE of a Si solar cell, while the overlap with the (broad) absorption function is small. These are near-ideal properties in combination with LSCs. The overall efficiency found in the 12 cm $\times$ 12 cm $\times$ 0.3 cm slabs connected to silicon PV was 1.02% for the LSC10, that absorbs 10% of incident light and contains 0.3 wt% QDs, and 3.27% for the LSC20 slab, that absorbs 20% of incident light and contains 0.5% QDs.

In this work we use CuInS$_2$-ZnS core-shell QDs, kindly provided to us by dr. Chenghui Xia, who synthesized the QDs as part of his research in the Condensed Matter and Interfaces group, at Utrecht University. For more information, see A.1 and [43].
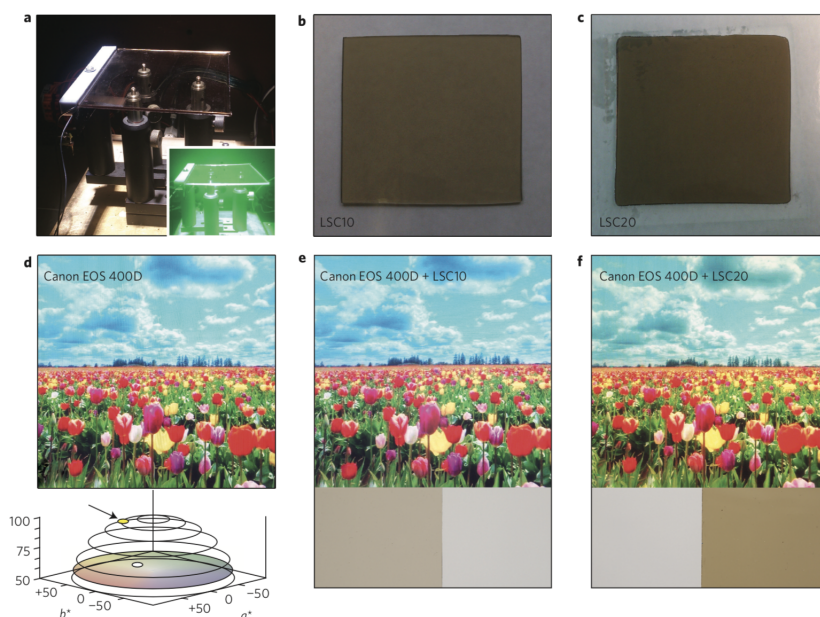

FIGURE 2.7: The pictures demonstrate the transparency and colourlessness of the CISeS based LSCs. (a) photograph of the setup during PCE tests, (b) and (c) show the 12 $\times$ 12 $\times$ 0.3 cm^3 slabs with a concentration of 0.3 wt% (LSC10) and 0.5 wt% (LSC20), respectively. The names refer to the percentage of incident radiation that are absorbed. The second row contains photographs taken with a camera without a filter (d), through the LSC10 (e), and through the LSC20 slab (f). The lower pictures are taken with the same LSCs covering half of the white background that is photographed. (g) shows the colour coordinates in the CIE colour space of LSC20 (the white circle), compared to a device based on a yellow organic dye (yellow circle). These pictures were taken from [29].
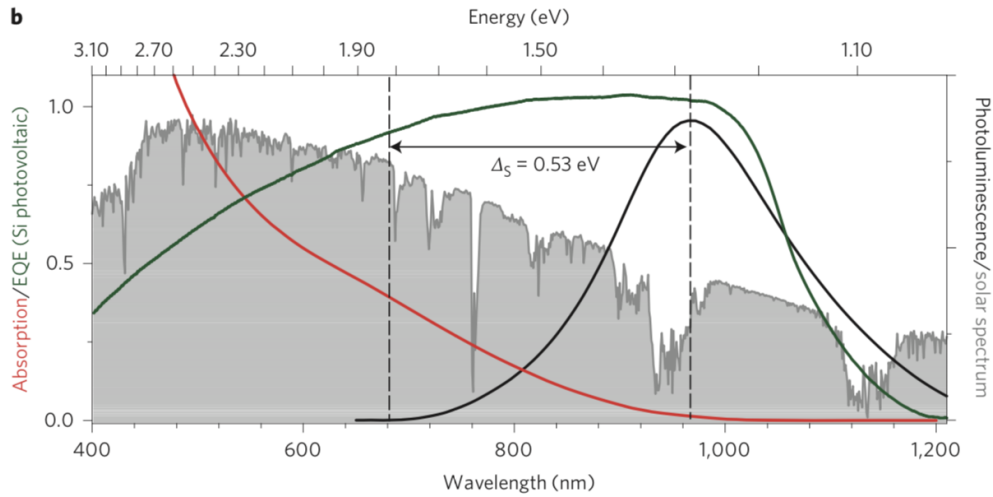
FIGURE 2.8: Absorption (red line) and emission (solid black line) spectra of ZnS-coated CISeS QDs in a toluene solution together with the EQE of the matched (silicon) solar cell. The stokes shift is indicated by the dashed lines. This figure is taken from [29].

The major remaining losses in QD LSCs are related to the luminescence quantum yield (Φ_{PL}) and light escaping through the escape cone. Φ_{PL} varies between different materials and is partially suppressed upon implementation in the matrix material. For instance, the Φ_{PL} of Si QDs drops from 50±5% in toluene to 46±5% when embedded in poly(lauryl methacrylate) (PLMA) crosslinked with ethylene glycol dimethacrylate (EGDM) [29]. Other types of QDs, such as CuInSeS and CdSe, need additional passivation coatings when incorporated in poly-acrylate matrices but exhibit high efficiencies of >70% [29, 42]. The polymers that are generally used in combination with semiconductor QDs, such as PLMA and PMMA, have a refractive index of close to 1.5, which, by Snell's law, means that approximately 74% of the light emitted by the photons is totally internally reflected. They come with the advantage that the absorption spectrum lies almost entirely in the infrared and shows little overlap with that of the QDs, therefore there is almost no parasitic absorption [30].

As the escape cone is generally the major mechanism through which photons are lost, reducing this loss can significantly enhance the performance of LSCs. Since this loss occurs after every absorption and re-emission, the total loss through this mechanism affects emitters with a small Stokes shift, and thus high reabsorption, more strongly. The most common approach to reduce escape cone losses is the implementation of selective mirrors. Aligning the luminophores can also reduce escape cone losses. This was earlier limited to organic emitters that are dichroic in their absorption and transmission, but now research is focused on the directional emission of self-aligned of nanorods [19]. More exotic shell designs that enhance absorption and direct emission of the dots are also theoretically investigated, but the practical realization of such structures is uncertain, if not impossible [41].

Although selective mirrors can effectively trap light in the waveguide, they fail to guide the light into the TIR modes [12]. This means that the light inefficiently propagates towards the edges of the waveguide, increasing the probability of any of the other loss mechanisms to occur. Here, we propose a novel approach to prevent light

from escaping the waveguide. By coupling the quantum dots to resonant nanostructures, designed to match their absorption and emission spectrum, the emission pattern can be altered. This pattern is normally isotropic when averaging over an ensemble of QDs. The structures can be tuned to suppress emission below the critical angle for TIR, allowing us to minimize this loss.

3 Resonant Dielectric Nanostructures

3.1 Theoretical background

The optical properties of a particle are closely related to its size, shape, and material. This precise relation gives rise to a vast range of possibilities to tune these features. Though *all* scattering can be traced back to the same physical principles, namely the acceleration of the discrete electric charges of which matter is composed by an external electromagnetic field, the specific optical properties are strongly correlated with the *size* of the particle [6]. In particular, a (sub)wavelength scale structure can exhibit optical resonances that enhance the interaction with light [22]. For visible light, this implies that the structures are in the order of 100 nm. The type of resonances that are supported and the wavelengths at which these occur are strongly related to the geometry and material of the particle.

Both metallic and dielectric particles exhibit resonant behavior when they are sufficiently small, although they rely on distinct underlying phenomena. Free electrons in metal particles are collectively set in motion upon illumination by incident electromagnetic waves. The resulting resonances are called *plasmon resonances* and are associated with strong losses due to parasitic absorption in the metal. Dielectric resonators do not suffer from these losses because their resonances are displacement current loops as opposed to actual current loops [22].

The absorption and scattering of light in spherical particles of arbitrary radius can be described analytically using Mie theory, after Gustav Mie [31]. Hence the terms *Mie-scattering* and *Mie-resonances*, that are more loosely used for non-spherical particles exhibiting similar behavior. These particles cannot be described analytically, but Mie-theory does provide a good tool to study many of the optical effects that occur in small particles [6]. The field scattered by a particle can be written as a multipole expansion, where the coefficients weigh the contribution of the various normal modes.

Because of the increased local density of optical states (LDOS) for particles on resonance, the scattering cross-section increases with respect to the geometrical cross-section. The ratio between these cross-sections, Q_{scat}, gives a measure of the light-matter interaction. Moreover, distinct modes have distinct far-field radiation patterns. These patterns are generally generated by a superposition of normal modes which can interfere constructively or destructively. Directional emission is based on this interplay. Depending on the propagation and polarization of the light radiated by distinct multipoles, light can interfere destructively in one direction, while interfering constructively in another direction, depending on their relative phase [24]. By tweaking particles' geometry such that they support specific modes at certain wavelengths, it is then possible to guide the light in a desired direction.[1]

---

[1]Note that intentional directional behavior does not necessarily happen at resonance frequencies, but rather when the conditions are such that multiple modes interfere constructively or destructively in a direction of choice [38].

It should then come as no surprise that these resonators are a captivating subject of study, both for fundamental research as well as for practical applications. The latter applies to this research project. With the current methods in nanofabrication, it is possible to precisely make these tiny particles to control and manipulate light at the nanoscale. This has lead to a variety of applications. Dielectric nanostructures, in particular, have been successfully employed in solar cell designs to enhance absorption and reduce reflection [7]. Plasmonics have proven less fruitful in this field due to the earlier mentioned losses although they are gaining attention.

Here, we will study the scattering behavior of TiO$_2$ cylinders in a medium with a 1.5 refractive index, close to that of LSC waveguides. The choice for TiO$_2$ is based on its high refractive index and low absorption. The modes supported by these cylinders are less pronounced than those found in their silicon counterparts in air due to the lower contrast in index.

3.2 Simulations

As discussed in the previous section, an analytical description of resonators is limited to spherical particles. To study the behavior of our cylindrical nanoparticles we thus have to resort to numerical methods. To identify the optimal geometry for the resonators we use finite-difference time-domain (FDTD) simulations in Lumerical [18]. The purpose of these resonators is twofold: to enhance absorption of the incoming (sun)light in the blue and to direct the emission of the quantum dots in the red into the TIR modes. The Stokes shift of the QDs helps overcome problems regarding reciprocity. Van de Groep and Polman [21] provided a comprehensive and systematic study of the resonant behavior of high-index dielectric particles through numerical simulations. We roughly follow their procedure to find and match the resonances to the spectral properties of our emitters. We use TiO$_2$ for the resonators for its relatively high refractive index, ~2.4 at 600 nm wavelength, but absorption close to zero for wavelengths longer than 400 nm. For resonances to occur, a contrast in the refractive index between the resonator and the background is needed. Note that we are designing specifically for use in LSCs, and the resonators will thus be embedded in a roughly 1.5 index medium (i.e. the waveguide). These material constraints (transparency of the resonators, together with the 1.5 index medium) cause the resonances to be less pronounced than in higher index (such as silicon) resonators in air. This is due to the relatively poor mode confinement and therefore higher radiative losses [21].

Because of the dual function of our resonators, we rely on two parallel simulation procedures to quantify their resonant qualities. In both procedures, we use a cylinder with a refractive index value that is measured with ellipsometry (see A) and set the background index to 1.5 and take it to be lossless, i.e. the imaginary part of the index is equal to 0. The mesh is varied according to the degree of precision that is needed for the specific simulation.

To determine the optimal geometry for directional emission, we run simulations with an electric point dipole, that resembles the quantum dot emission, oriented along the x-axis, located at the center of the cylinder, as in figure 3.1. Using a `scat_ff` box, we can extract the far-field intensity of the radiation. The power emitted into the solid angle $d\Omega$ is given by the time-averaged Poynting vector [35]
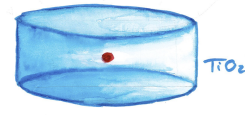

FIGURE 3.1: Quantum dot in the center of a TiO$_2$ cylinder.

$$dP_{sca} = \frac{1}{2}\sqrt{\frac{\epsilon_0\epsilon_d}{\mu_0}}|E_{sca}|^2 r^2 d\Omega, \qquad (3.1)$$

with ϵ_0 the dielectric constant in vacuum, μ_0 the vacuum permeability, and ϵ_d the relative dielectric permittivity of the surrounding medium. We then calculate the ratio between power emitted outside the escape cone and the total scattered power by

$$\frac{\int_0^{2\pi}\int_{\theta_{crit}}^{\pi-\theta_{crit}}|E_{sca}|^2\sin\theta d\theta d\phi}{\int_0^{2\pi}\int_0^{\pi}|E_{sca}|^2\sin\theta d\theta d\phi}. \qquad (3.2)$$

This gives us a measure of the directive efficiency of the structure. We use this in a brute-force parameter sweep over a range of cylinder heights and diameters. The ratios found for each of the geometries are plotted in figure 3.2. We see that a resonator with a 610 nm diameter and 200 nm height most efficiently directs the light outside of the escape cone, namely with a ratio of 0.94. In comparison, this ratio is 0.68 for a horizontal dipole *without* a resonator. Henceforward, unless specified otherwise, we assume the nanoparticle to be of this form.
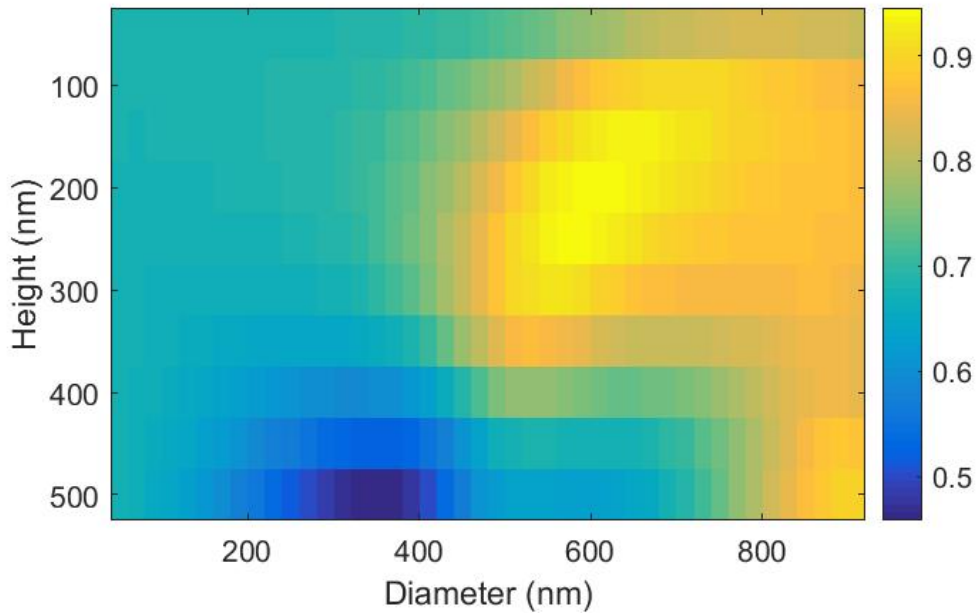

FIGURE 3.2: The ratio between emission outside the escape cone and total radiated power of a dipole of 900nm wavelength oriented along x in the middle of a TiO$_2$ cylinder with varying height and diameter.

Let us now have a look at the radiation pattern of this resonator to gain a better intuition of how light is guided into the TIR modes of a waveguide. We do this by comparing them to the radiation pattern of a dipole in the background medium

without the resonator, see figure 3.3. The two lobes indicate a complete suppression of light emitted in the z-direction while emission along the y-axis is enhanced. This is referred to as *side scattering* [35].
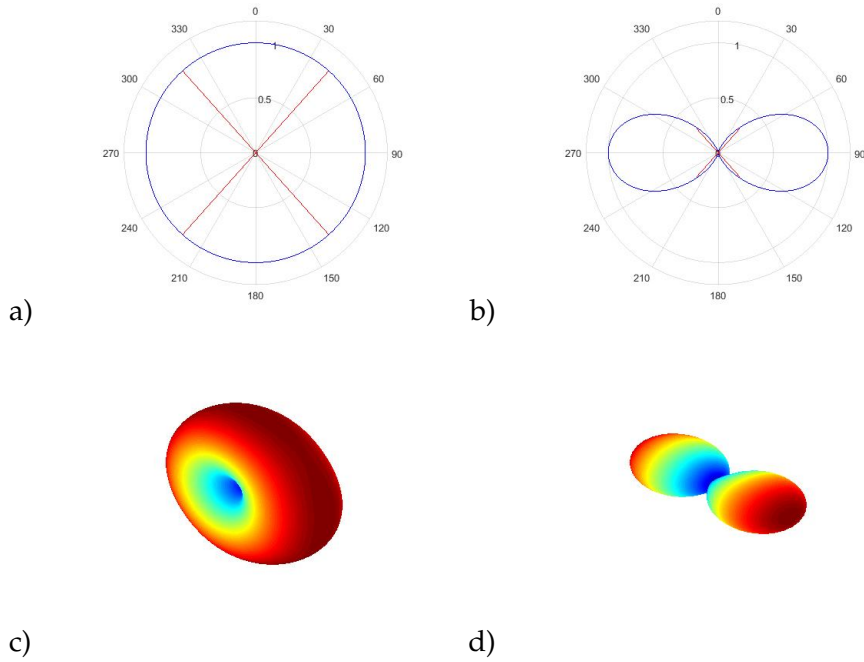

a)

b)

c)

d)

FIGURE 3.3: Radiation distribution in the yz-plane of a) a dipole oriented along x in air, b) a dipole oriented along x in a TiO$_2$ resonator. The red lines indicate the escape cone. c) and d) simply give a three dimensional representation of the situation above.

Next to the radiation pattern, analyzing the field profiles of the resonators can give us a better insight into the modes that govern the particle's behavior. At the moment of excitation, the dipole dominates the fields in the structure. We, therefore, use the method of apodization to filter out this component. This means that a slight delay is induced in the sampling so that the dipole has stopped radiating but the excited modes are still present. In this case, the apodization center lies at 100 fs and has a width of 20 fs. Note that this is a rather sensitive procedure: a few femtoseconds later and the fields are gone, while a little earlier the dipole is still dominating.

Looking at figure 3.4 we see that the field-profile somewhat resembles that of an anapole, which is a composition of the electric and toroidal dipole moments. However, the anapole mode is radiationless due to the destructive interference of the similar far-field scattering patterns of its components [32]. Anapoles can moreover be identified by a characteristic dip in the scattering cross-section at the point where the electric and toroidal contributions are equal.[2] This is not the case here. Rather, from the radiation pattern, we expect a contribution of the magnetic quadrupole together with the total electric dipole, which is the combination of the toroidal and electric dipole [5, 35].

We compare these fields to those induced by a plane wave of the same wavelength of 900 nm, see figure 3.4. The field profiles induced by an x-polarized plane wave propagating in the z-direction closely resemble those induced by the x-oriented dipole. This is probably due to the dominant contribution of the x-dipole, and the x-polarized light couples to this mode. A decomposition of the multipoles could give

---

[2]See [32] for more information on anapoles in dielectric nanoparticles.

further insight into the other contribution modes [17]. However, this is not (yet) possible with a dipole excitation.
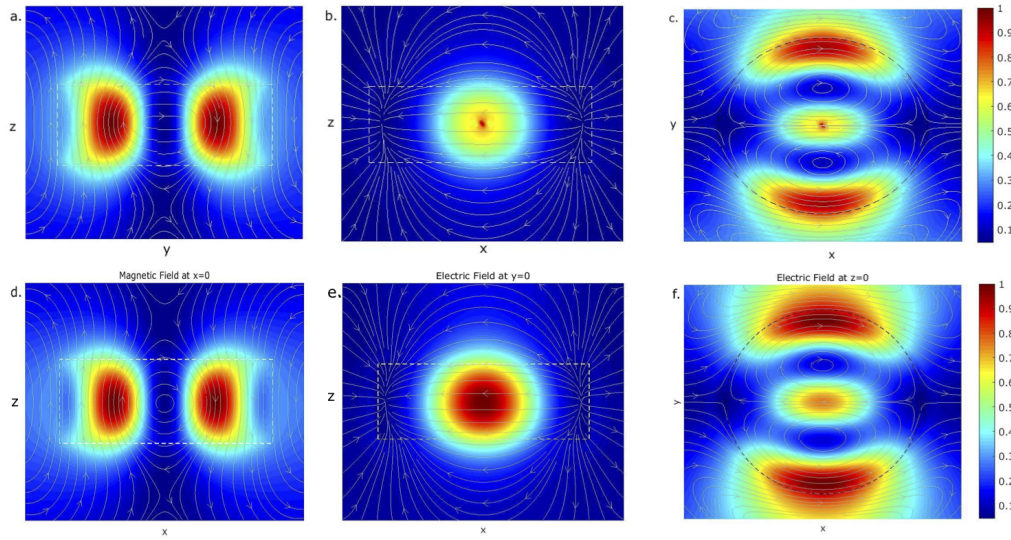

FIGURE 3.4: Field profiles in a 200nm high cylinder with a diameter of 610nm excited by a plane wave propagating along z (top row) or an electric point dipole (bottom row) located in the center of the cylinder, both polarized in x. The dashed lines indicate the edges of the particle.
a. and d. show the normalized magnetic field together with the magnetic field lines in cross-cuts of the cylinder at x = 0, b. and e. show the electric field at y = 0, and c. and f. show the normalized electric field intensity together with the electric field lines at z = 0.

The same procedure was repeated for a vertical dipole, which already has a near-ideal radiation pattern for LSCs. In figure 3.5 the radiation pattern is shown for the dipole with and without the optimized cylinder. We see that the far-field intensity does not change drastically, the characteristic donut shape is preserved. However, it does flatten slightly, thereby radiating even less within the escape cone. Examining the field profile we see that the electric dipole is still the dominant mode, as one would expect from the radiation, see figure 3.7. Here we also compared the fields to those induced by a plane wave with the same polarization, for which we do not find the same similarities as for the horizontal dipole.

We finally check the total radiated power per wavelength for both a vertical dipole and a horizontal dipole at the center of the cylinder and compare this to the power radiated by a single dipole in the background medium without the resonator. This gives an indication of the resonance wavelengths of the structure when excited by a dipole source. Moreover, as directive behavior does not necessarily happen at resonance wavelengths, it is possible that the total scattering is low [38]. However, as shown in figure 3.6, the total radiated power is enhanced as compared to a dipole in the background medium. We do see that the desired directive properties do not happen at peak resonance frequencies.

As we have the intention to embed multiple QDs in a single resonator, it logically follows that the majority of them will not be at the center of the resonator. The coupling efficiency is determined by the overlap of the electric fields of the dipole with the eigenmodes of the resonator [22]. Therefore we examine the position dependence of the directive efficiency. We do this by shifting the dipole position from the center of the cylinder towards the side and top. Due to rotational and mirror symmetry, we only do this in one quadrant of one plane. Moreover, while it was

a)   b)

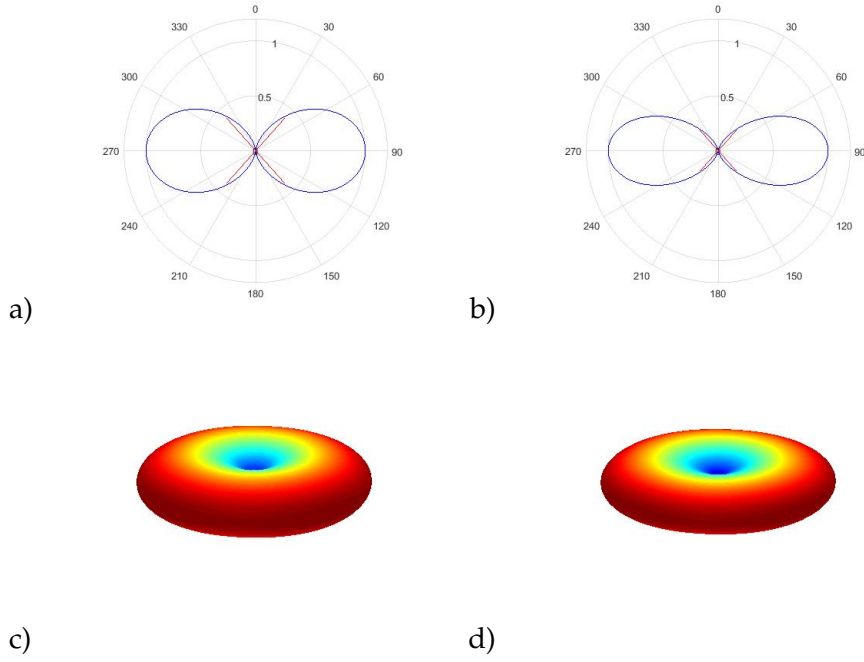c)   d)

FIGURE 3.5: Analogue of figure 3.3 but for a vertical dipole. Radiation distribution in the yz-plane of a) a z-oriented dipole in air, b) a dipole oriented along z in a TiO$_2$ resonator with d = 610 nm and h = 200 nm. The red lines indicate the escape cone. c) and d) simply give a 3 dimensional representation of the situation above
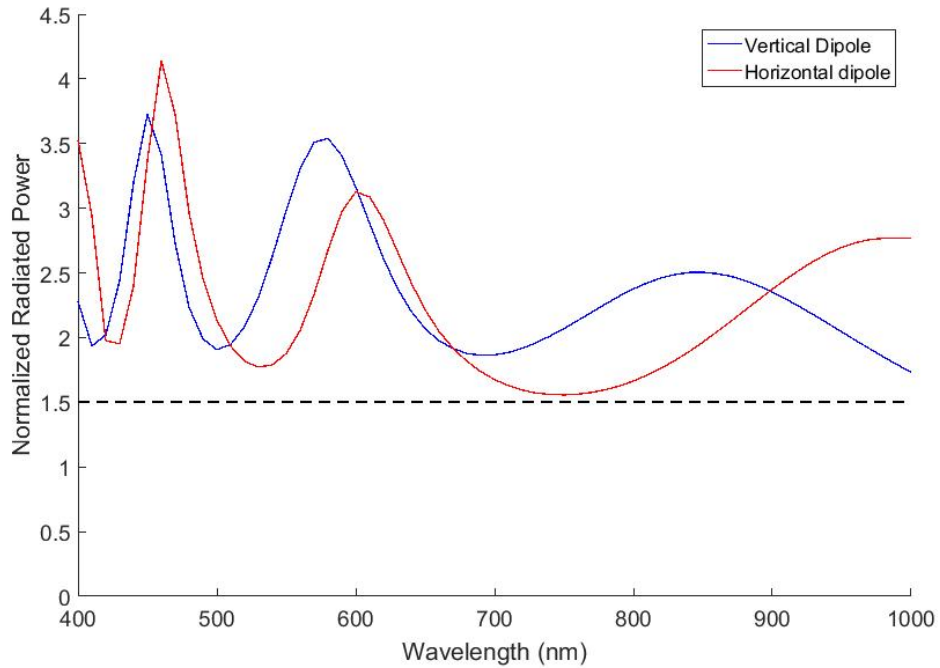

FIGURE 3.6: Total radiated power of a vertical and horizontal dipole embedded in the resonator, normalized to the power radiated by a dipole in free space, as a function of the wavelength. The directive properties we are interested in happen at a wavelength of 900 nm, exactly where the two graphs cross. The radiated power is enhanced by a factor 2.35, when compared to a dipole in the lossless 1.5 background medium, indicated by the dashed line.
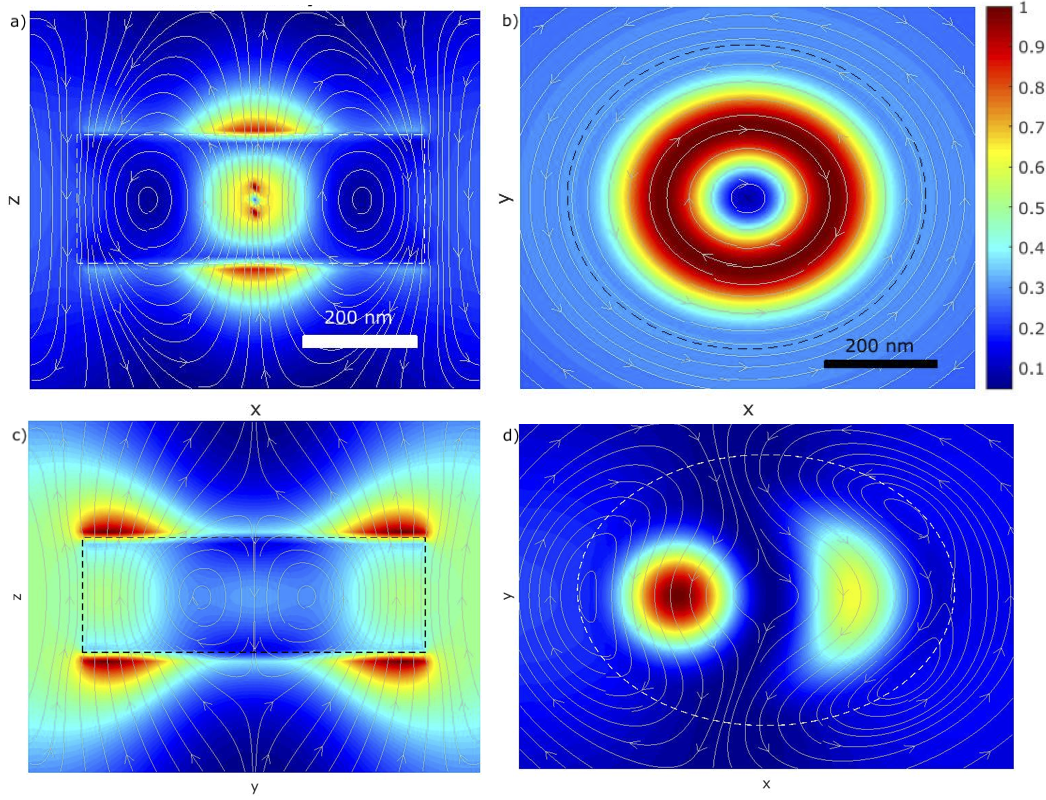
FIGURE 3.7: a) the normalized electric field intensity at y = 0 is plotted with the electric field lines induced by a vertical electric point dipole, b)the normalized magnetic field along with the magnetic field lines at z = 0 for the same configuration, in c) the normalized electric field intensity and electric field lines at y = 0 with a z-polarized plane wave excitation along x, and d) the electric field intensity and lines for the same plane wave excitation at z = 0.

justified to only use an x-polarized dipole in the first optimization because of rotational symmetry, we now use three orthogonal dipoles (along x, y, and z) and for each position determine the average emission ratio. A crosscut of the cylinder with the average emission ratio for each of the position is shown in figure 3.8.

Based on this configuration, a final simulation is run with three orthogonal electric dipoles (in separate simulations) shifted from the center of the cylinder towards the side. This is done at three distinct heights, evenly spaced in the layer where the quantum dots will be placed. For the refractive index and thickness of this layer we use ellipsometry data of a spin-coated layer of $CuInS_2$-Zn core-shell quantum dots, emitting at 875 nm, see appendix A.1. Again, the emission ratio is calculated for each position and weighted according to the distance from the central axis of the cylinder. Moreover, the shape of the particle is designed to imitate the structures as fabricated in section 4.1. This results in an average of 85% of the light being emitted outside the escape cone in a waveguide with an index of 1.5, as opposed to 74% without the resonator. The overall radiation pattern is simulated by using the same weighting procedure and rotating the exported field around the axis. This is depicted in figure 3.9 together with the simulation space.

To examine the scattering efficiency, the structures are excited from the top by a plane wave, to mimic the incoming sunlight. This is a limited imitation, as sunlight will not just come in at normal incidence and has different polarizations. However, this cannot be solved by simply rotating the incoming field, as the total field
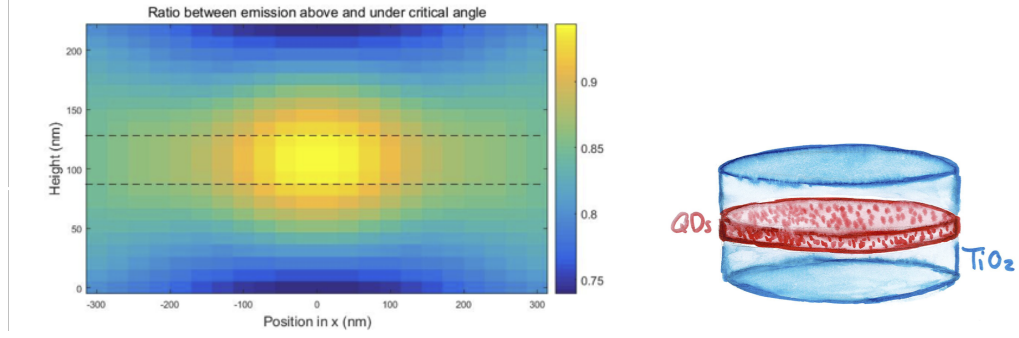
FIGURE 3.8: On the left: a crosscut of a cylinder, showing the ratio between light emitted outside the escape cone and the total radiated power in all angles per position. Averaged over three orthogonal dipoles. From this figure, it is clear that the light is most efficiently directed outside the escape cone and into the guide modes for QDs in the middle of the nanoparticle. Therefore, the structures will be made by sandwiching a layer of QDs in between two layers of TiO$_2$, as shown on the right where the final design of the structure is depicted. A d = 610 nm, h = 200 nm cylinder, composed of two 80 nm thick layers of TiO$_2$ with a 40 nm layer of QDs sandwiched in between.
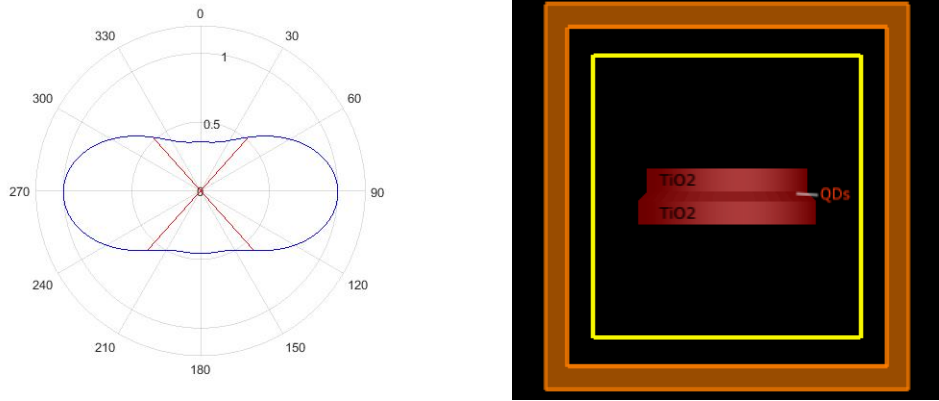

FIGURE 3.9: On the left the simulated far field radiation distribution of a 34 nm thick layer of QDs in the nanoparticle as shown on the right. Here, 85% of the light is emitted outside of the escape cone, which is indicated by the red lines.

scattered field (TFSF) source and the perfect matching layers (PML) as boundaries that we use are optimized for normal incidence. The parameter of interest is the scattering cross-section, σ_{scat}, which we normalize by dividing it by its geometrical cross-section, σ_{geo}, to get

$$Q_{scat} = \frac{\sigma_{scat}}{\sigma_{geo}}, \tag{3.3}$$

this in turn provides information on the absorption efficiency. For a Q_{scat} higher than 1, caused by an increase of the LDOS, the resonator effectively functions as a funnel for the incoming light.

For clarity, we first have a look at the wavelength-dependent scattering efficiency of silicon resonators in air. These support clearly defined electric and magnetic modes, that are indicated by peaks in the Q_{scat}, see figure 3.10 [21]. The modes that correspond to these peaks can be identified by studying the field profile in the resonator for specific wavelengths at which these peaks occur, analogously to the case dipoles excitation at wavelengths that give the desired directivity for LSCs.
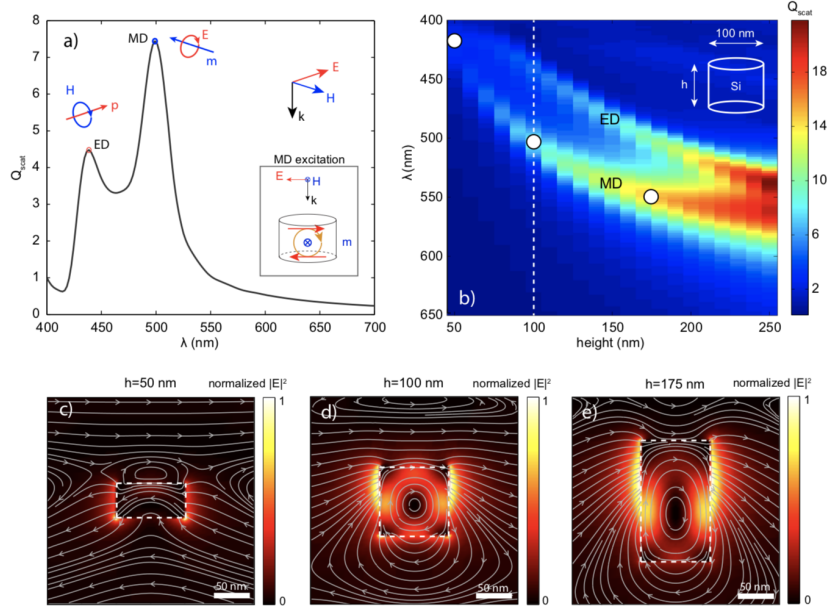
FIGURE 3.10: Fig. 1. (a) Q_{scat} as a function of the wavelength for a Si cylinder in air with h = 100 nm and d = 100 nm excited by a plane wave under normal incidence. The peaks correspond to the electric dipole and magnetic dipole modes. The polarization of the driving field is shown in the top right. (b) Q_{scat} (color) as a function of the wavelength and cylinder height. The vertical white line is the crosscut corresponding to the spectrum shown in (a). The white dots correspond to the configurations used for (c-e). (c-e) Normalized electric field intensity $|E|^2$ (color) and electric field lines (gray) in vertical crosscuts through particles with h = 50 nm (c), h = 100 nm (d) and h = 175 nm (e), parallel to the electric driving field. This figure and was taken from [21]
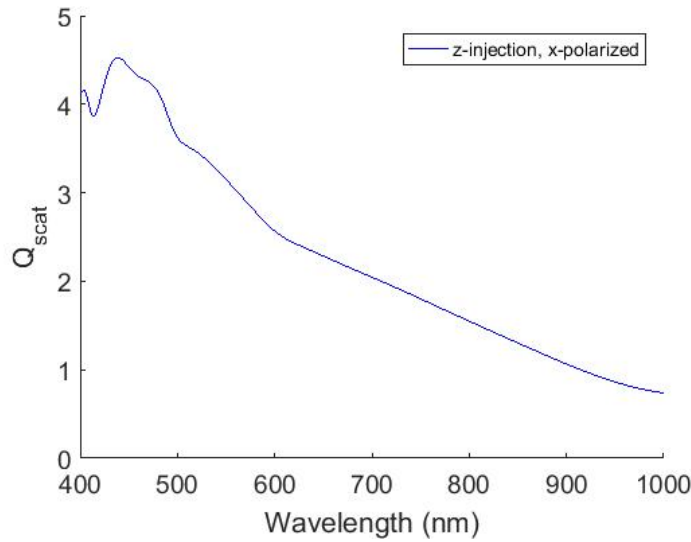

FIGURE 3.11: Q_{scat} as a function of the wavelength for the optimized cylinder in a waveguide, excited by an x-polarized plane wave injected along the z axis.

Similarly, the scattering efficiency of our design can be determined. The resulting efficiencies are plotted in figure 3.11. However, in this case, we do not learn much

from a study of the fields corresponding to the peaks in the graph. Instead, we see again that a multipole decomposition is necessary to provide more information on the contributing modes.

What *is* evident from the field profiles is that a combination of higher-order multipoles together govern the higher scattering cross-section for the wavelengths between 400 nm and 500 nm. See figure 3.12 for an example such a field profile. We want to enhance absorption, i.e. get a Q_{scat} greater than one, in the absorption range of the QDs. The current design gives a Q_{scat} close to four for the wavelengths at which the QDs most efficiently absorb.[3] The pitch at which the resonators are spaced will hence be equal to four times the diameter. Because of the large size of the pitch no collective lattice modes or grating

FIGURE 3.12: Crosscut at x = 0 of the cylinder with a 450 nm x-polarized plane wave excitation, propagating along z.

effects are expected to appear. In our fabrication, they are distributed on a square grid, but a hexagonal lattice provides a better way to evenly cover the plane. See figure 3.13 for a simplified picture of how the resonators may be embedded in a device.
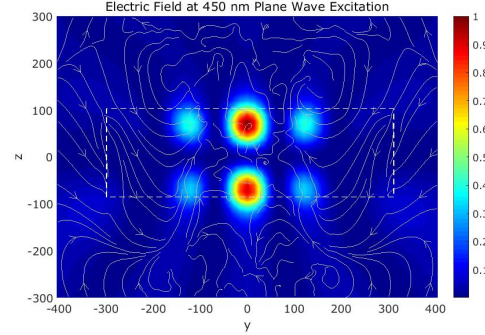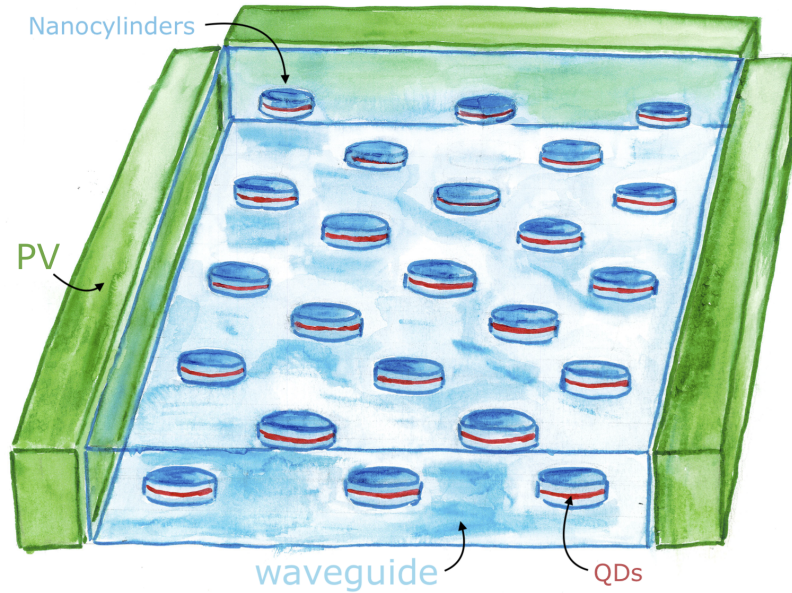

FIGURE 3.13: A simple graphical presentation of the nanocylinders embedded in an LSC device.

---

[3]see A.1

4 Experimental Realization

There are several examples of successful integration of quantum dots in a patterned design but it is not a trivial task. Successful implementations include procedures that rely on solgel in combination with nanoimprint lithography, structures that consist entirely out of quantum dots developed with a wet etching method [26], through sputtering of SiO$_2$ and Si and consecutive etching [8] and a waveguide with quantum dots sandwiched in between that was realized with an RIE etch [44]. The emphasis of this project and chapter is on the final fabrication procedure. For completeness, we will mention alternative approaches that were tried but did not work and pathways that have potential but have yet to be explored in section 4.3. Note that the substrates of use were generally made out of silicon because this significantly eases intermediate monitoring of the fabricated structures through ellipsometry and scanning electron microscopy (SEM). Apart from checking the geometrical and material properties of the structures during the process, perhaps the most crucial part of the fabrication is to preserve the luminescence of the QDs. It is, therefore, necessary to carefully keep track of the PL between the various steps in the fabrication procedure to know how they affect the QDs.

The choice of materials was fairly straightforward, TiO$_2$ is known for its relatively high refractive index and low absorption. Patterning this material is known to be a bit of a hassle, but it is not impossible as we show in the following section.

4.1 Top Down Fabrication Procedure

We settled for a top-down fabrication procedure based on Ha et al. [23] of which all the consecutive steps are depicted in 4.1. The TiO$_2$ layers are grown by EBPVD, which provides a fairly quick and easy way to make high-index amorphous TiO$_2$. We will now go through all of the fabrication steps in the chronological order of fabrication. First, the glass or silicon substrates are cleaned with a base piranha solution (not depicted). Next, (4.1,1) the substrates are brought into a vacuum chamber and positioned above a crucible with a precursor, in this case, Ti$_3$O$_5$. This precursor evaporates upon heating with an electron beam and precipitates onto the substrate. The base pressure of the chamber is 1×10^{-7} and is raised to 2.5×10^{-5} by letting in 1.5 sccm of O$_2$. The oxygen flow partially determines the final material composition.[1] The deposition rate can be adjusted by varying the beam current and is set to 0.2 nm/s. This corresponds to a beam current of roughly 75 mA. The desired thickness depends on the QDs and substrate that is used. This was determined with the method described in 3.2, for various dipole wavelengths and substrate specifications. The thickness is verified with a reflection based measurement with the Filmetrics system. The QD solution is then spin-coated for 40 s at 2500RPM onto the TiO$_2$ and dry baked at 60°C for 15 minutes. To remove dirt and large clusters from the solution we use a 0.2 μm filter on the syringe used to drop the QDs onto the substrate. See 4.2 for optical images of the resulting layers.
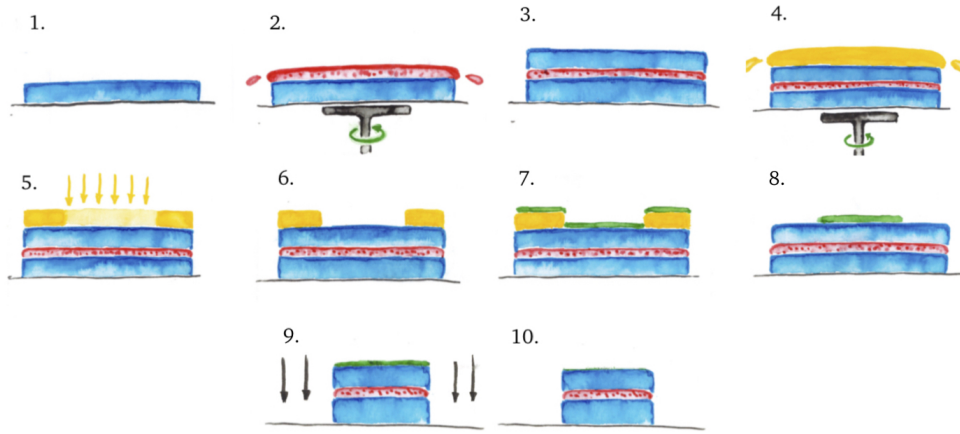
---

[1] see A for ellipsometry data of an oxygen test.

FIGURE 4.1: Fabrication steps 1. E-beam evaporation of TiO_x on a glass or silicon substrate. 2. Spin-coating 30-40 nm layer of CuInS-ZnS core-shell quantum dots. 3. E-beam evaporation of the second layer of TiO_x. 4. Spin-coating 110-120 nm PMMA. 5. Patterning of the structure by E-beam lithography. 6. Development of the PMMA by MIBK:IPA 7. E-beam evaporation of 25 nm Cr. 8. Lift-off by sonication in acetone. 9. RIE etch with CHF_3 and O_2 as etch gases. 10. Wet etch with Cr etchant.
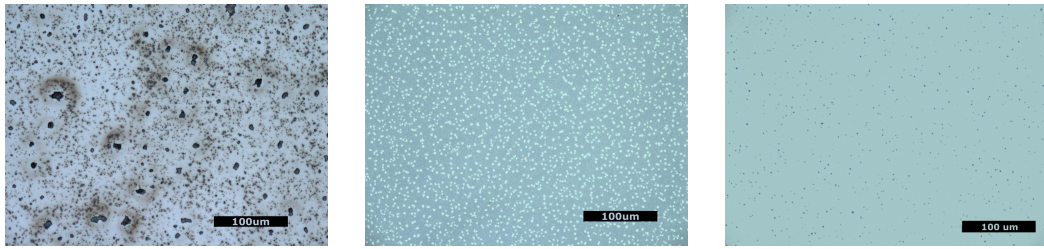

FIGURE 4.2: Optical microscope captures of unfiltered (left) and filtered 590 nm emitting (middle) and 875 nm emitting (right) $CuInS_2$-ZnS core-shell quantum dots, spin-coated on silicon.
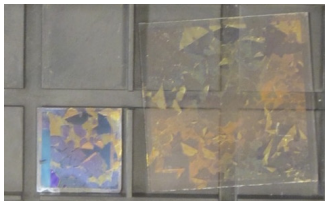

FIGURE 4.3: Shattered TiO_2 after spin coating PMMA.

In step 3 of 4.1 a second layer of TiO_2 is then evaporated on the QD layer following the same procedure as in the first step. The thickness is measured on a bare silicon substrate that undergoes the same evaporation recipe. When evaporated on the NIR emitting $CuInS_2$-ZnS QDs issues concerning surface stress of the TiO_2 arose, resulting in cracks [1]. This, in turn, led to problems in the next step (4.1, step 4) where we spin-coat a 110nm thick layer of PMMA (A8 950 1:2 in anisole). Figure 4.3 demonstrates the problem, which was partially solved by an intermediate anneal step at 200°C for an hour.[2] The PMMA was spin-coated at 4000RPM for 45 seconds followed by a 5-minute bake at 150°C. For glass substrates an extra layer of E-spacer was spin-coated on the PMMA, to improve conductivity. This was done for 40 seconds at

---

[2]Although this did not make the cracks in the TiO_2 disappear, it did prevent the shattering as shown in the picture. Issues regarding the surface tension of TiO_2 thin film are common and a more elaborate study on the influence of temperature, evaporation speed, and the substrate could help overcome these issues [10].

2000RPM and post-baked for 2 minutes at 90°C

Next (4.1, step 3), the PMMA layer was patterned by electron beam lithography with a 50 kV acceleration voltage. A narrow range dose test between 550 and 650 $\mu C/cm^2$ was always done on a 5×5 grid of 100×100 μm write fields. The pattern consists of an array of disks that define the size and shape of the Cr mask and thus the final cylinders. The pitch is equal to four times the diameter of the cylinders, and the precise dimensions vary according to the calculated geometry for the specific quantum dots and substrates, see 3.2.

After exposure, the glass samples are rinsed with water to remove the E-spacer, for silicon this is not necessary as no E-spacer is involved. In step 6 the PMMA is developed in a solution of methyl isobutyl ketone (MIBK) and isopropyl alcohol (IPA) in a ratio of 1:3, respectively for 90 seconds under constant movement. It is then rinsed in IPA twice for 15 seconds each and dried under a stream of N_2.

The substrates are then transferred to the Polyteknik EBPVD system to deposit the Cr mask (4.1, step 7). This procedure is roughly the same as in steps 1 and 3, just without the oxygen flow and with Cr in the crucible. We evaporate 25 nm of Cr at a rate of 0.1 nm/s. The following lift-off (4.1, step 8) is done by ultrasonication in acetone twice for 5 minutes, followed by 1 minute of sonication in IPA. Note that this procedure works well when the QD solution is not filtered but after filtering large parts, if not all, of the top layer, are stripped off the sample. Using a megasonicator instead of an ultrasonicator could avoid this problems. Another approach is to soak the substrate into a preheated (80°C) resist stripper (PRS-3000) for 20 min under constant agitation of a magnetic spinner [26]. Figure 4.4 shows an SEM image of the finalized Cr mask.
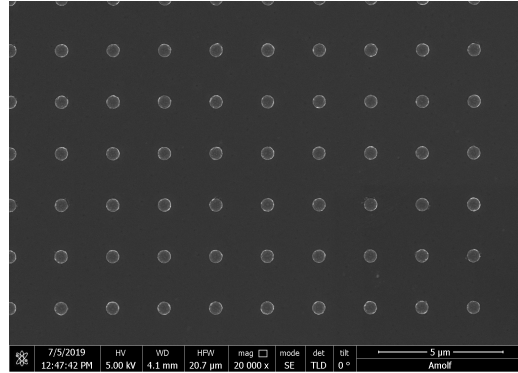

FIGURE 4.4: SEM image of the Cr mask

We etch down the cylinder using a reactive ion etch (RIE) system with CHF_3 and O_2 as etch gases (4.1, step 9) with a flow of 50 sccm and 1 sccm respectively, to get close to vertical sidewalls. See section 4.2 for more information on the optimization of the recipe, etch rates and theory of this etching procedure. The final step in the fabrication (4.1, step 10) is then to remove the Cr mask. This is simply a matter of dipping the sample into a ceric ammonium nitrate-based Cr etchant for 15 seconds, rinsing with water and drying under a stream of nitrogen. SEM images of the finalized structures, before and after the Cr etch, are shown in figures 4.5 and 4.6. Note the dips in the surface around the pillars that only happen with the 580 nm emitting QDs. This can probably be attributed to the slightly less homogeneous QD layer, as can be seen in figure 4.2.
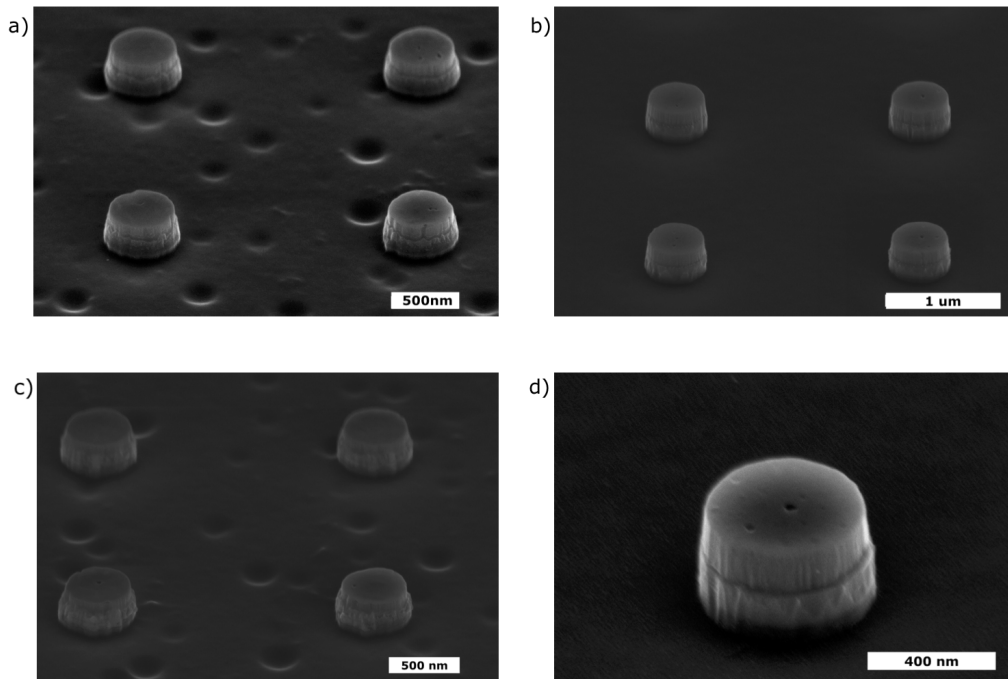
FIGURE 4.5: SEM images of a) four pillars of TiO$_2$ with a layers of 580 nm emitting QDs before the Cr etch, b) four pillars of TiO$_2$ with a layers of 875 nm emitting QDs before the Cr removal, c) the same pillars as in a) but after the Cr etch, and finally d) a close up of 1 as in c) after removal of the Cr mask.
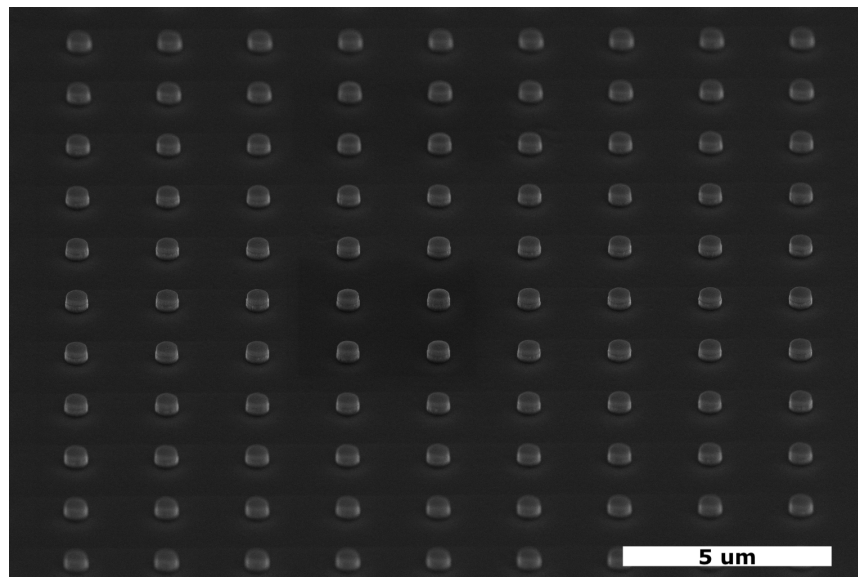

FIGURE 4.6: SEM image of an array of nanopillars with 875 nm emitting QDs.

4.2 Etching of TiO$_2$

The optical properties of TiO$_2$ make it a desirable material for a wide range of applications. Despite its beneficial qualities, it is a challenging material to work with in nanofabrication. There are several known bottom-up fabrication procedures but these come with a limited degree of freedom in the design and it is not possible to combine these with a layer of quantum dots in the structure. A plasma etch based top-down fabrication method helps overcome some of the limitations that are imposed in bottom-up procedures. However, TiO$_2$ is notoriously difficult to etch due to a lack of volatility of its etch products. Anisotropic etching of TiO$_2$, in particular, can be a cumbersome task. Luckily, Hu et al. [26] have conducted a systematic study of various combinations of gases provided elaborate documentation of the influence on the etch rates and sidewall angles. Using this as a starting point we have optimized the recipe for the Oxford Instruments PlasmaLab80 RIE etching system with the available gases on our amorphous TiO$_2$ films, see table 4.1 for the final recipe. Apart from determining the right combination and ratio of gases the mask needs to have a sufficiently high selectivity, which is especially important in the fabrication of nanostructures with a high aspect ratio. This is more difficult than in similar materials such as SiO$_2$ and Si$_3$N$_4$ due to the harsh etching conditions that are required [26]. Cr offers a high selectivity and though the deposition of the mask is a cumbersome task (see 4.1) it does the job well. The Cr etchant that is used to remove the mask does not affect the TiO$_2$ but slightly etches the QDs. This is not problematic as this merely results in the removal of QDs that are deposited on the sides of the structure, probably due to sputtering in the etch step. Initial characterization and optimization was done with all TiO$_2$ structures and later tweaked with the intermediate layer of QDs. We now observe a broadening in the structure at the level of the quantum dot layer. The degree of enlargement is dependent on the QDs and the thickness of the layer, as is to be expected. The sidewalls also seem slightly slanted in the entire structure. This could perhaps be reduced by etching without O$_2$ to reduce passivation of the sidewalls. In all-TiO$_2$ structures this resulted in a slight underetch. Moreover, only single-step etch procedures were tested. A 3-step etch process with, for example, Ar added in the gas mix for the quantum dot layer could result in more efficient etching of the middle layer due to increased sputtering. Although tests with Ar showed increased sidewall roughness, that could, in turn, lead to scattering losses [44], while some broadening still occurred. Also, perfectly straight sidewalls are nice but not necessary for the functionality of the resonators, as is tested in FDTD simulations of the fabricated structures in section 3.2.

CHF$_3$	50 sccm
O$_2$	1 sccm
Ar	0 sccm
Forward Power	200W
Pressure	37.5 mTorr
T	20°C
Etch rate	9 nm/min

TABLE 4.1: Optimized recipe for TiO$_2$ etching.

4.3   Alternative routes

Aside from the final fabrication method, as presented above, we explored two other ways of fabrication; by atomic layer deposition (ALD), a sol-gel method. The advantage of using a high-index (TiO_2 based) sol-gel is that imprinting does not require many steps, but can be done with a fairly simple nano-imprint procedure. However, mixing quantum dots with the sol-gel often requires a ligand exchange for the transfer from a non-polar to a polar solvent. This generally comes at the cost of some loss of PL [43]. For a proof-of-concept, such as in our case, this does not directly impose big problems. However, the sol-gels we managed to produce here were not very suitable for imprinting and required an annealing step to raise the, otherwise low, refractive index [16]. This, in turn, ruined the photoluminescence of the quantum dots.

Atomic layer deposition is a method that allows a high level of control over the material. Through this method rutile, anatase, and amorphous TiO_2 can be fabricated, depending on the precursors and temperatures used during the process. Additional annealing steps can increase the crystallinity and index of the material but aren't required. Moreover, it was demonstrated that it can be precisely patterned [15]. Unfortunately, the reaction between the two precursors, H_2O and $TiCl_4$, that we used instantly diminishes all of the photoluminescence of the quantum dots. Note that this does not happen for all ALD processes. PL is, for example, preserved after the atomic layer deposition of AlO_x, see A.1.

5 Measurements

Measurements on the samples were initially executed to keep track of the photoluminescence of the QDs. After the full experimental realization of the structures, the obvious next step is to measure the directive properties and the change in absorption. In the next section 5.1 the PL measurements are presented. Directive measurements were attempted with a Fourier microscope but unfortunately hampered by the sensitivity of our setup, or lack of PL, depending on how you like to look at it. Alternatively, we present preliminary cathodoluminescence spectroscopy data in section . Note that these are just exploratory measurements and should be regarded with caution. No final conclusions can and should be drawn from these results.

5.1   Photoluminescence

The photoluminescence of the quantum dots was measured using a WITec Alpha300 RS microscope. A schematic of the setup is depicted in figure 5.1. A 405 nm laser was used to excite the 560 nm emitting CuInS$_2$-ZnS core-shell QDs.
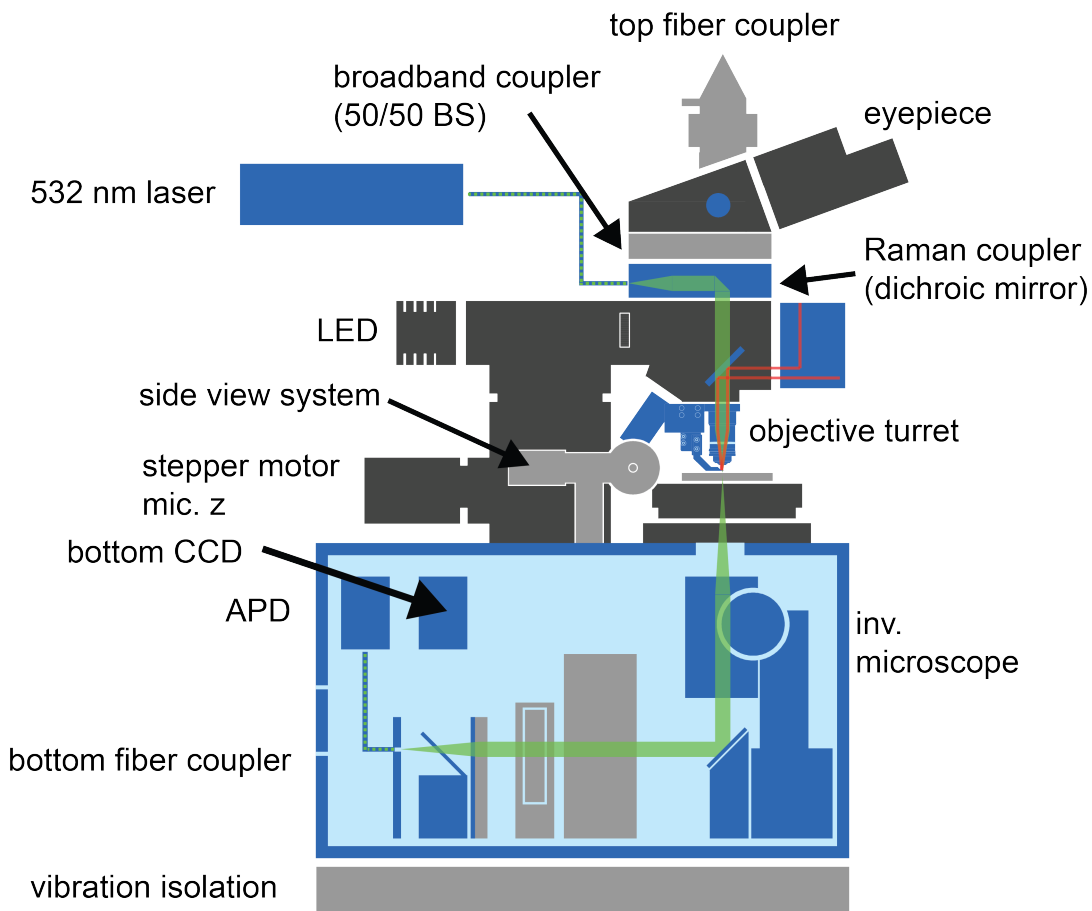

FIGURE 5.1: WITec Alpha300 RS microscope.

The laser is coupled in with a broadband coupler and then focused on the sample through a 50x Zeiss Epiplan objective with a 0.8 NA. This means that it collects light emitted within an angle of 53°. The light is then collected from the sample and passed through a 488 nm long-pass filter to filter out the reflection of the laser. The remaining light is then sent to a spectrometer through a UV-VIS fiber. Note that these measurements do not tell us the PL quantum yield but only disclose whether some of the PL is preserved. On single samples, the intensity of the signal fluctuates heavily if the quantum dot layer is not homogeneous. Samples with quantum dots that were filtered before spin-coating give a fairly constant signal all over the substrate. Without prior filtering, however, there were large deviations in the number of CCD counts. Even when averaging over multiple line scans on each sample we only use these as an indication of whether the quantum dots survive the fabrication steps at all. For this reason, we do not include the intermediary steps, as PL after the final step indicates the presence of PL in all of the preceding steps.

During the research, these measurements were crucial tests to see the viability of the various procedures. See section 4.3 for some of the routes with a dead-ending due to the absence of PL. Moreover, the spectral shape that we see when measuring $CuInS_2$-ZnS core-shell QDs on a substrate (regardless of the substrate's material composition) is different from the PL spectrum of the same QDs in solution. For more information see A.1.
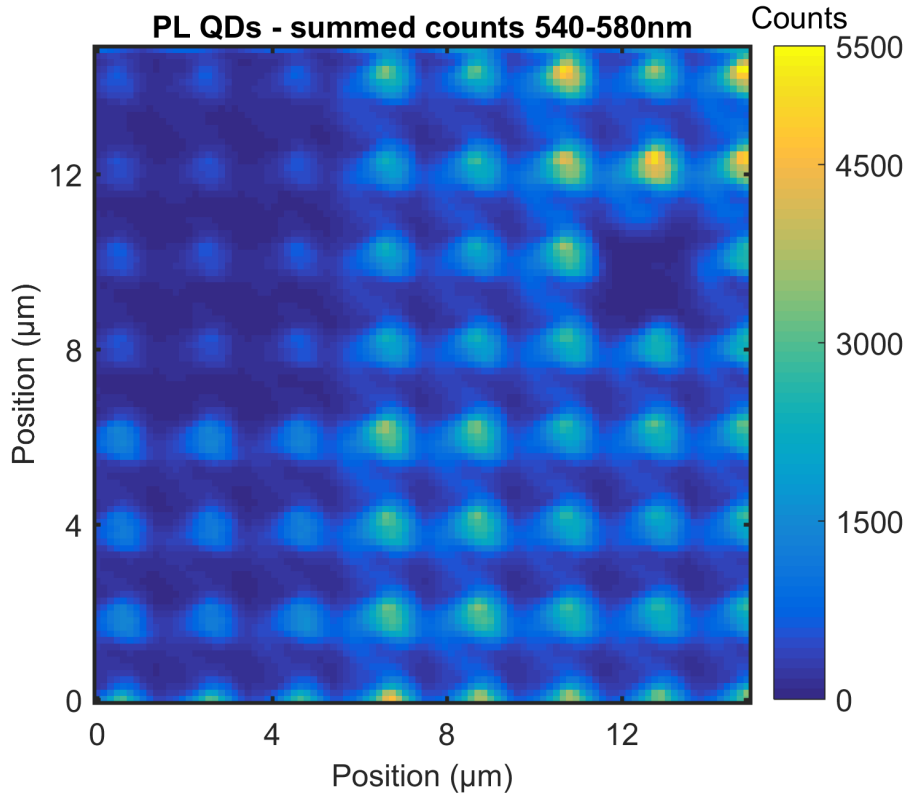

FIGURE 5.2: A spectral map over an area of 15×15 micron of cylinders, indicated by the yellow square in figure 5.3. Each pixel corresponds to a spectrum. The color indicates the number of CCD summed counts at the peak of the emission spectrum of the QDs: between 540 nm and 580 nm.

In figure 5.2 we present a spectral map of a sample with pillars that consist of two 130nm thick layers of amorphous TiO_2 with a layer of QDs sandwiched in between, fabricated on a silicon substrate. The diameter of the pillars is roughly 520nm distributed on a square lattice at a 2080nm pitch. The map was taken over an area of $15 \times 15 \ \mu m^2$, with a total of 10.000 measurement points, each 150nm apart on a 100×100 grid. On each of the points, the spectrum is accumulated 1 second. Note that there is no significant photobleaching, during the measurement on each point the spectrum remains nearly the same. Each of the pixels on the

FIGURE 5.3: Optical image of the measured sample, the yellow square indicates the area over which the spectral map was taken.

map corresponds to such an accumulated spectrum. The color represents the number of CCD counts in the peak of the QD spectrum; between 540nm and 580nm. Figure 5.6 shows a spectrum that corresponds to one of the pixels on the map. The
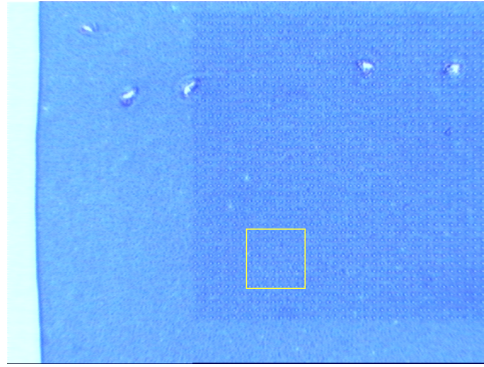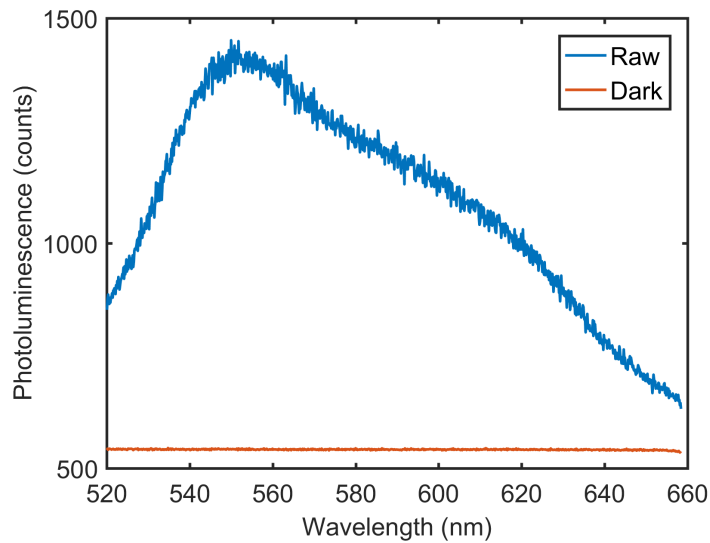

FIGURE 5.4: Spectrum corresponding to a single pixel in the map in figure 5.2.

map clearly indicates the presence of the QDs in the pillars. This is evident from the correspondence between the optical image and the map in terms of the grid as well as from the spectral shape that matches that of the earlier measured QDs on a bare substrate or in between two layers of TiO_2 but before patterning, see A.3. Moreover, we do not measure a signal when measuring TiO_2 pillars without the embedded QDs. If the emission is indeed directed mostly above the critical angle for TIR, then we expect a lower number of counts than before patterning (due to the NA of the objective). This indeed seems to be the case. But again, we use the set up as a measure for the presence of PL, not to determine a quantum yield or, in this case, the directivity. The signal simply fluctuates too much for those kinds of conclusions. Also, a reduction in PL could simply mean that the QDs have lost part of their luminescence.

5.2   Cathodoluminescence

To determine the directive properties of the fabricated cylinders a preliminary angle-resolved cathodoluminescence (CL) measurement was executed. This was done on the same sample that was used for the spectral map, as shown in figure 5.2. There are no reference measurements, so these only serve as a first indication for the directive behavior of the pillars. For this reason, we will not go into detail on the theory. See [11] for more information on angle-resolved CL spectroscopy.

In CL an electron beam is used to excite the sample. The acceleration voltage determines the penetration depth. In figure 5.5 we see a small bump in the spectrum around 550 nm for excitation on the pillar. This could indicate that this signal comes from the QDs. Figure **??** then shows the far-field intensity at 550 nm wavelength for various excitation positions. When exciting close to the center of the pillar the emission is mostly directed to the sides. The dashed line indicates the critical angle for TIR of a 1.5 index medium in air.
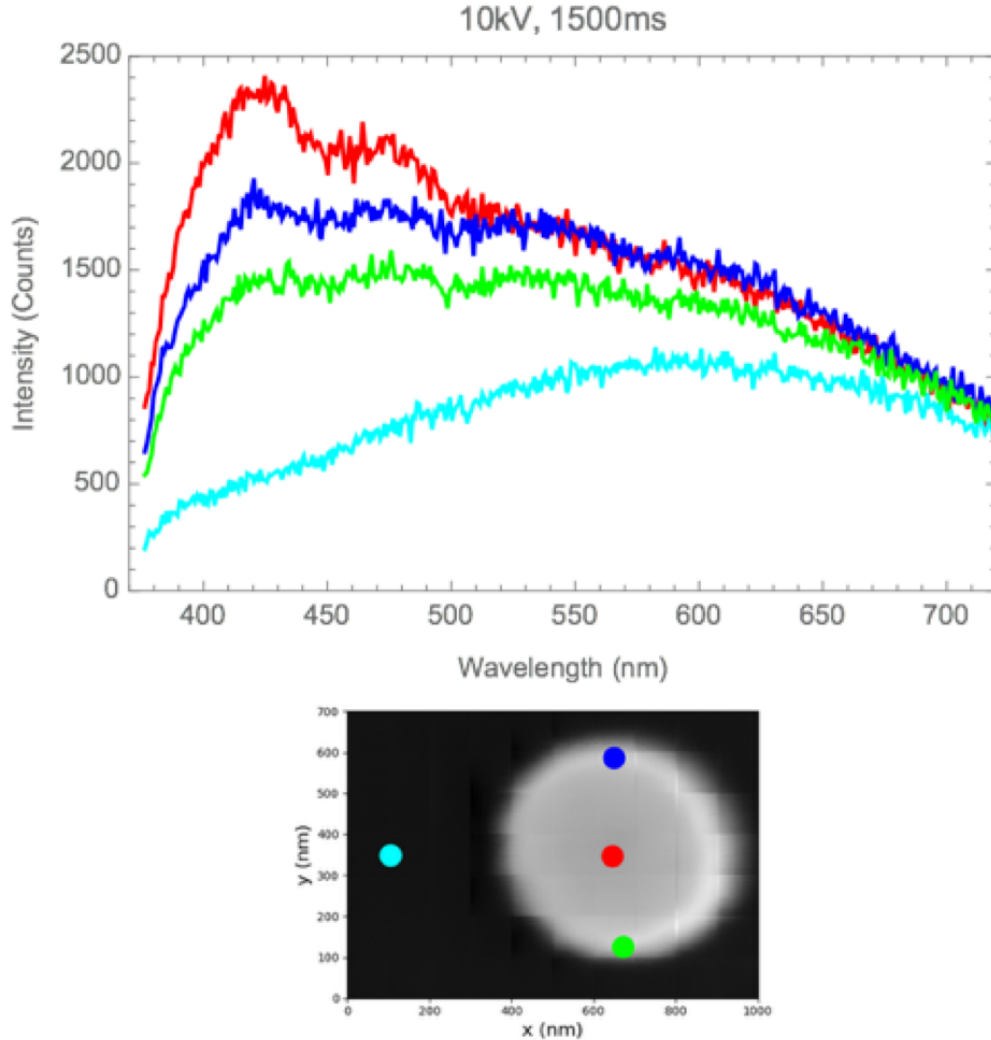

FIGURE 5.5: Position dependent CL spectra. The colors of the spectra correspond to the colored dots on the SEM image below. These indicate the excitation spots.
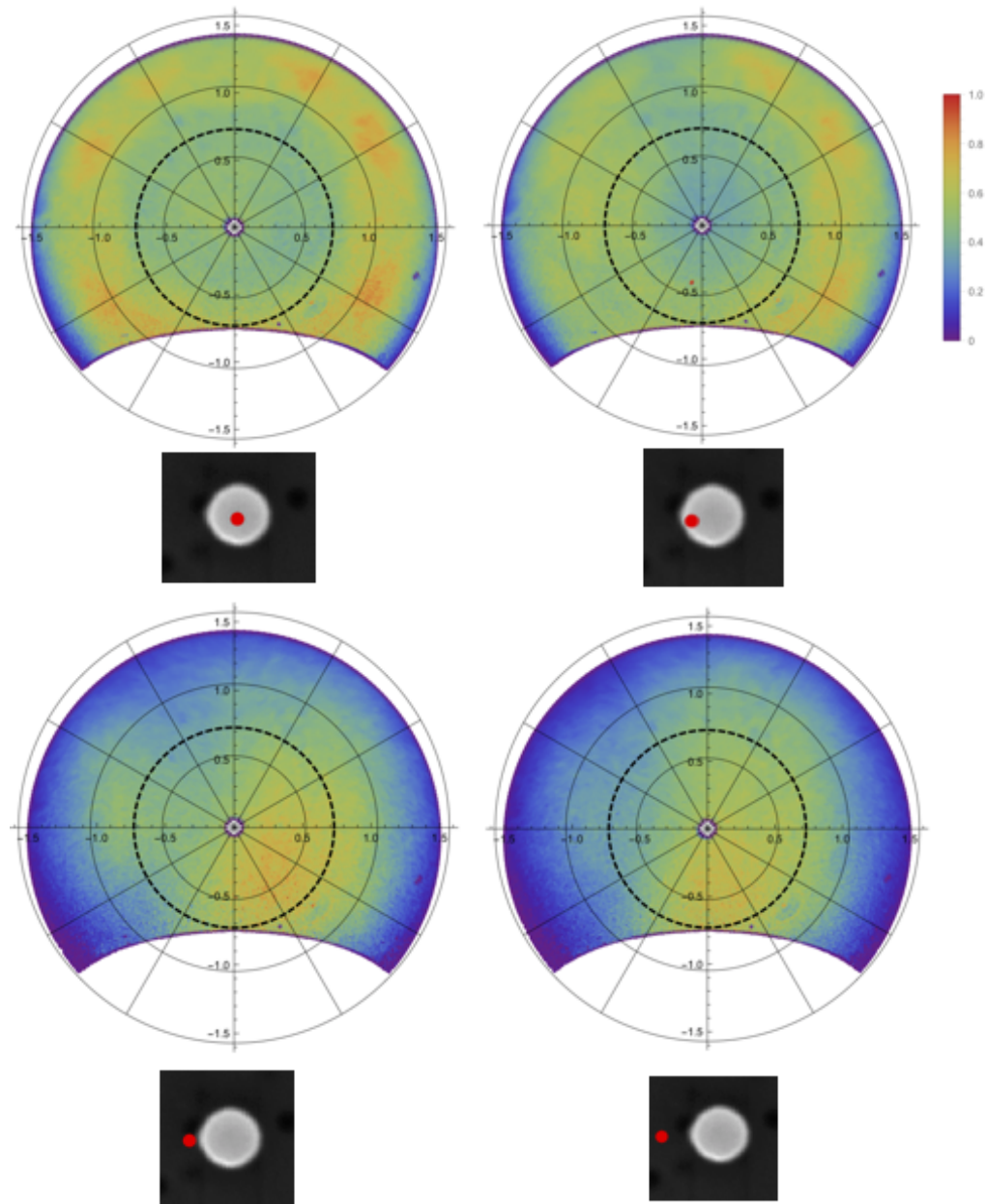
FIGURE 5.6: Normalized far field intensity at 550 nm wavelength. The sample was excited with a 10 kV electron beam. The SEM images below each plot indicate the excitation spot. The dashed line indicates the critical angle for TIR of a waveguide in air.

6 Discussion

Based on experimentally measured parameters, we have designed resonant dielectric nanostructures that effectively suppress emission below the critical angle in a 1.5 index waveguide. This was done with a brute force algorithm. Although the field profiles, radiation pattern, and scattering efficiency of these particles were studied, a more solid understanding of the contributing modes was not yet attained. As stated in 3.2, a multipole decomposition is a well-known method to derive these contributions for resonators excited by a plane wave. Unfortunately, we did not manage to finalize this within the given time. Moreover, in general, a decomposition of this kind does not apply to dipole excitations.

We have thus far only looked at the behavior of a single resonator in a medium with an index similar to that of the waveguide. Our design is aimed at the implementation of an array of nanostructures distributed in an LSC. Although we have demonstrated enhanced absorption and directed emission for a single structure, we do not yet know how the presence of the nanostructures will influence the propagation paths of the emitted photons. Monte-Carlo ray-tracing simulations are normally performed to analyze these pathways, but because of the employment of nanostructures, we reside in the wave-optics domain.

Perhaps these mechanisms are best studied experimentally, as the overall system becomes rather complex. To do so, a logical next step is to fabricate structures with QDs with the 'right' absorption and emission functions. With 'right' we mean NIR QDs, similar to those presented in figures 2.8 and A.2. These QDs with these properties, together with a sufficiently thick protective shell, were unfortunately not at our disposal during the performed experiments. Also, silicon substrates were useful during the optimization and testing of the fabrication procedure but finally the pillars need to be embedded in a waveguide. Now that most of the optimization on silicon has been done, minor adjustments (specifically in the E-beam lithography) need to be made for the fabrication on glass. Once this is completed, directive measurement in transmission can be executed.

A Materials

A.1 Quantum Dots

The quantum dots were a very important part of our design and fabrication. In LSCs we seek to use QDs with a low overlap in absorption and emission function and a high photoluminescence quantum yield (see section 2.1). Additionally, for this project specifically, the QDs needed to be resilient to the various steps in the fabrication procedure. The quantum dots we used were $CuInS_2$-ZnS core-shell particles dispersed in anhydrous toluene (20 mg/ml). The dots that we mostly worked with had a thicker protective shell (about 5 monolayers), as shown in figure A.1. The absorption and emission spectra of these QDs in solution are shown in figure A.1. Clearly the spectral properties are different from those upon which we based
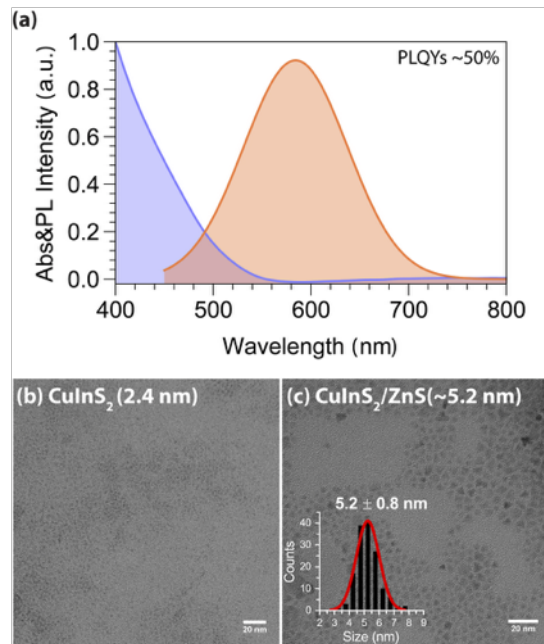

FIGURE A.1: a) Absorption and emission spectra 5.2 nm CuInS2-ZnS QDs with a PLQY of $50 \pm 2\%$. b) High resolution TEM images of CuInS2 core (~2.4 nm) and c) CuInS2-ZnS core-shell (~5.2 nm) QDs. The images show that the CuInS2 core QDs are coated by ~5 monolayers of zincblende ZnS. This figure was provided by Chenghui Xia [43].

the ideal resonator geometry. However, they did function well as test specimen and in principle it should be possible to synthesise similarly thick-shell QDs emitting in the NIR. We did have NIR emitting quantum dots composed of the same core and shell materials but with a thinner shell (1 or 2 monolayers as opposed to 5). See figure A.2 for its absorption and emission functions. However, multiple problems occurred when working with these particles. For one, after merely spin coating them on a silicon substrate the signal was rather low. This could in part be attributed to

the limited sensitivity of our CCD at longer wavelengths. We do not have the information on the grating response, but even after correcting for both the CCD and the objective we measured a spectrum that was not only low, but also blueshifted ~150 nm from the spectra that were measured on the same QDs in solution. This was measured with a different set-up, and it is therefore difficult to compare the two, but we can assume that such a large shift does not originate in measurement artefacts. A blueshift can be caused by the oxidation of the QDs. This is especially probable because of the thinner protective shell, which could prevent the ~590 nm QDs from oxidizing.
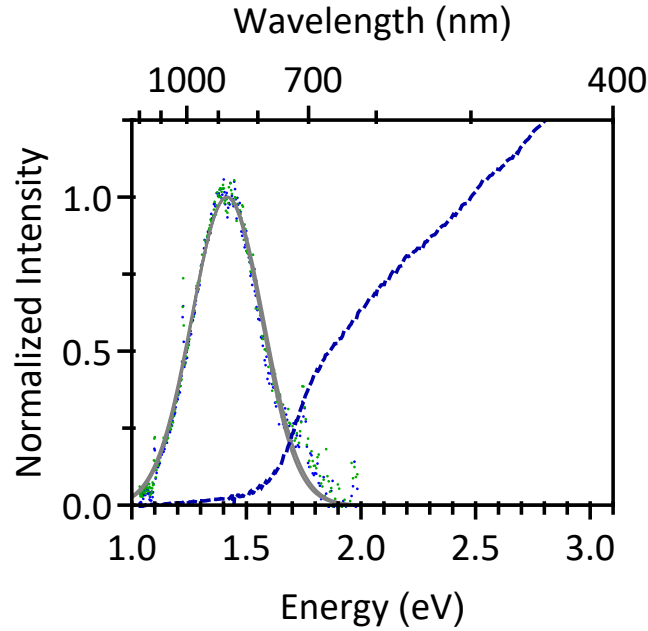

FIGURE A.2: Absorption and emission as a function of the photon energy
of the NIR CuInS2-ZnS QDS. Image courtesy of Tim Prins.

Also for the ~590 nm emitting QDs we observe a change in the spectral line shape and a blueshift. See figure A.3. This may be attributed to oxidation of a sub-population of the QDs, perhaps because of a variation in the shell-thickness. The thicker shell should normally prevent these effects from occurring. When depositing a thin (4 nm) AlO_x layer by ALD we do not observe the asymmetric line shape, but the emission function does broaden. Deposited layers of AlO_x have been used in combination with PbS quantum dots to prevent oxidation [27]. Other reasons for blue or red shifts in the emission spectrum are the enhancement of radiation channels for certain wavelength, as reported in [37]. However, as a similar shift is observed for various substrates, with and without the presence of resonators, this does not seem to be the cause.

A.2   Ellipsometry

Ellipsometry measurements were done with a WVASE J.A. Woollam system in order to determine the dielectric properties of the fabricated TiO_2 and QD layers. In ellisometry, a polarized light beam interacts with a sample, which induces a change in the polarization. This change is detected in the sample's reflection. We measure this reflection in three distinct angles, around the brewster angle. For the TiO_2 layers the measurements were done in a wavelength range from 300-1000 nm. For the QD
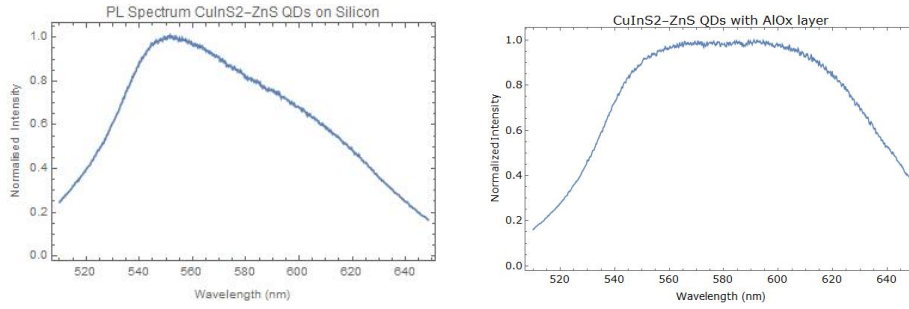
FIGURE A.3: On the left: PL spectrum of a layer of CuInS2-ZnS QDs, spin coated on a Si substrate. On the right: the same quantum dots, spin coated on a Si substrate, covered with a 4 nm layer of AlOx.

layer the reflection was obtained over a range from 300-1700 nm. After the measurement the raw data is fitted with a Cauchy model for a transparent film, for the QD layer we use this in combination with a Gaussian oscillator fit. The figures below show the refractive index and extinction coefficient of 80 nm thick thin films of TiO_2 that were obtained with this fit.
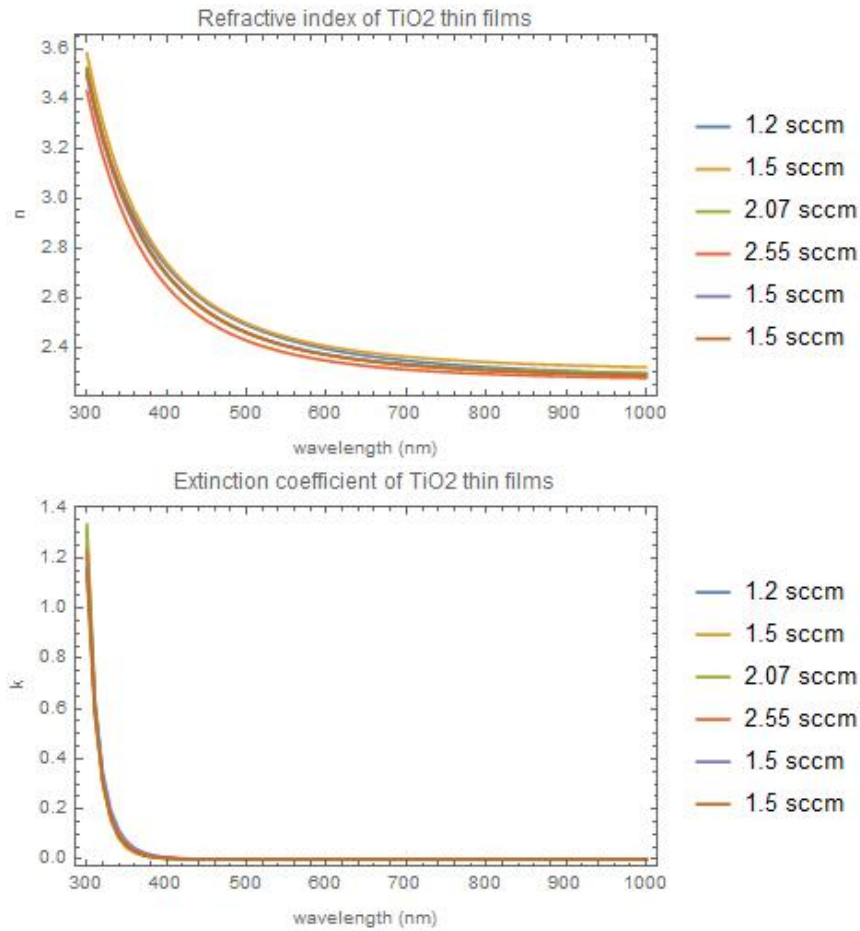

FIGURE A.4: Above: The refractive index of thin films of TiO_2 obtained with varying oxygen flows. Below: the extinction coefficient of the same samples.
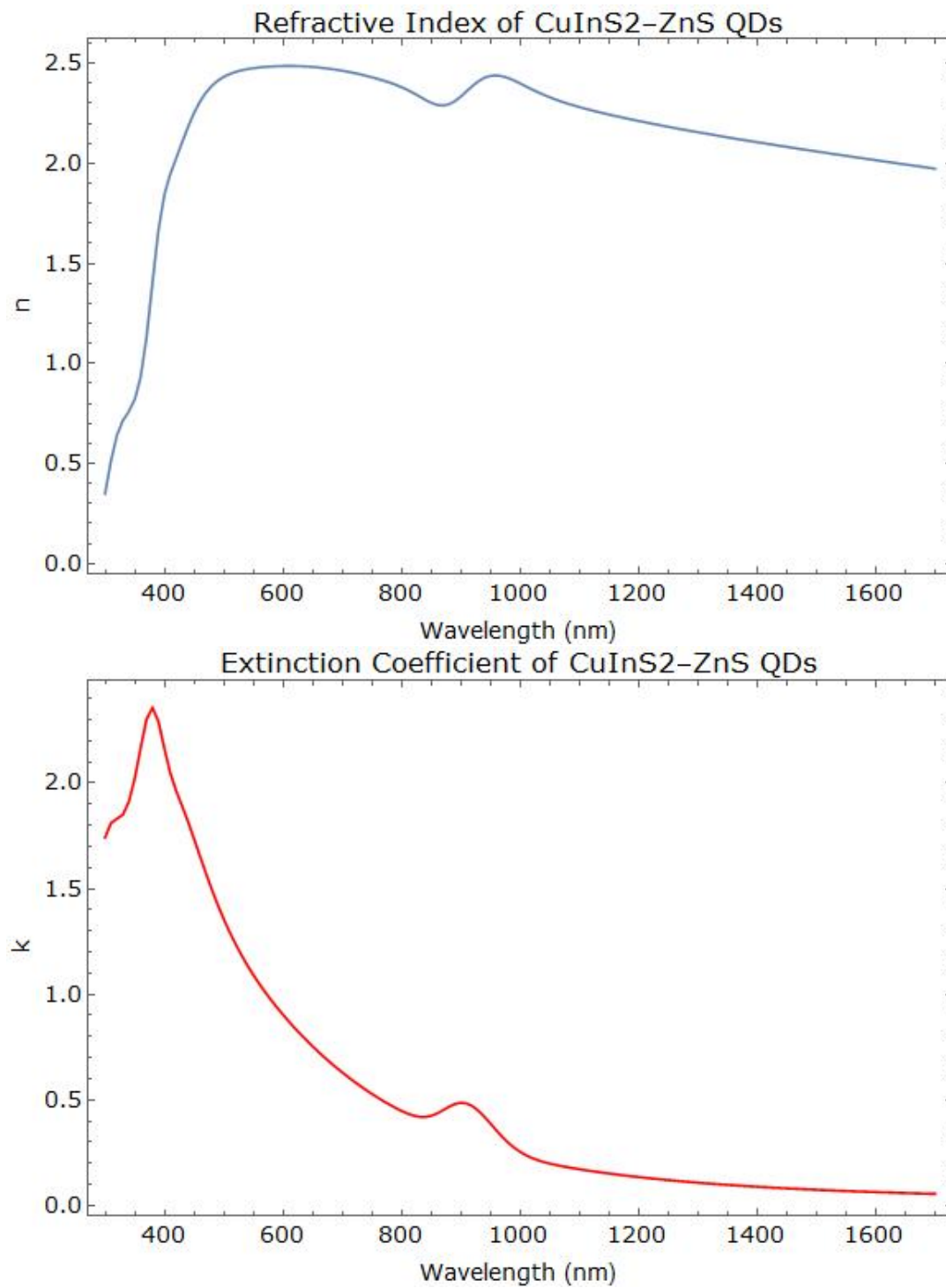
FIGURE A.5: The refractive index of a 33 nm spin coated film of 875 nm emitting $CuInS_2$-ZnS QDs.

Bibliography

[1] Grégory Abadias et al. "Review Article: Stress in thin films and coatings: Current status, challenges, and prospects". In: *Journal of Vacuum Science & Technology A* 36.2 (2018), p. 020801.

[2] Myles Allen, Barbiker Mustafa, and Priyadarshi Shukla. "Summary for Policymakers". In: *GLOBAL WARMING OF 1.5 C - an IPCC special report on the impacts of global warming of 1.5 C above pre-industrial levels and related global greenhouse gas emission pathways, in the context of strengthening the global response to the threat of climate change, sustainable development, and efforts to eradicate poverty* (Oct. 2018), p. 32.

[3] Svante Arrhenius. "XXXI. On the influence of carbonic acid in the air upon the temperature of the ground". In: *The London, Edinburgh, and Dublin Philosophical Magazine and Journal of Science* 41.251 (1896), pp. 237–276.

[4] Matthew R. Bergren et al. "High-Performance CuInS2 Quantum Dot Laminated Glass Luminescent Solar Concentrators for Windows". In: *ACS Energy Letters* 3.3 (2018), pp. 520–525.

[5] Andrey A. Bogdanov et al. "Bound states in the continuum and Fano resonances in the strong mode coupling regime". In: *Advanced Photonics* 1, 016001 (2019), p. 016001.

[6] C. Bohren and D. R. Huffman. *Absorption and Scattering of Light by Small Particles*. Ed. by C. Bohren and D. R. Huffman. Wiley Science Paperback Series, 1998.

[7] Mark L. Brongersma, Yi Cui, and Shanhui Fan. "Light management for photovoltaics using high-index nanostructures". In: *Nature Materials* 13 (Apr. 2014), 451 EP –.

[8] Antonio Capretti, Arnon Lesage, and Tom Gregorkiewicz. "Integrating Quantum Dots and Dielectric Mie Resonators: A Hierarchical Metamaterial Inheriting the Best of Both". In: *ACS Photonics* 4.9 (2017), pp. 2187–2196.

[9] Rachel Carson. *Silent Spring*. 50th Anniversary. Houghton Mifflin Harcourt, 2002 (1962).

[10] Hsi-Chao Chen, Kuan-Shiang Lee, and Cheng-Chung Lee. "Annealing dependence of residual stress and optical properties of TiO2 thin film deposited by different deposition methods". In: *Appl. Opt.* 47.13 (2008), pp. C284–C287.

[11] Toon Coenen. "Angle-resolved cathodoluminescence nanoscop". PhD thesis. 2014.

[12] Ryan Connell and Vivian E Ferry. "Integrating Photonics with Luminescent Solar Concentrators: Optical Transport in the Presence of Photonic Mirrors". In: *J. Phys. Chem. C* 120 (2016), p. 45.

[13]   World Energy Council. *Energy and the challenge of sustainability*. Sept. 2000. URL: http : / / www . undp . org / content / dam / aplaws / publication / en / publications/environment-energy/www-ee-library/sustainable-energy/ world-energy-assessment-energy-and-the-challenge-of-sustainability/ World\%20Energy\%20Assessment-2000.pdf (visited on 07/25/2019).

[14]   Michael G. Debije and Paul P. C. Verbunt. "Thirty Years of Luminescent Solar Concentrator Research: Solar Energy for the Built Environment". In: *Advanced Energy Materials* 2.1 (2012), pp. 12–35.

[15]   Robert C. Devlin et al. "High efficiency dielectric metasurfaces at visible wavelengths". In: (2016).

[16]   Pablo Docampo et al. "Efficient organometal trihalide perovskite planar-heterojunction solar cells on flexible polymer substrates". In: *Nature Communications* 4.1 (2013), p. 2761.

[17]   Andrey Evlyukhin et al. "Multipole analysis of light scattering by arbitrary-shaped nanoparticles on a plane surface". In: *Journal of the Optical Society of America B* 30 (Sept. 2013), p. 2013.

[18]   *FDTD Solutions | Lumerical Inc*. https://www.lumerical.com/.

[19]   Martyn Fisher et al. "Utilizing vertically aligned CdSe/CdS nanorods within a luminescent solar concentrator". In: ().

[20]   Jan Christoph Goldschmidt et al. "Increasing the efficiency of fluorescent concentrator systems". In: *Solar Energy Materials and Solar Cells* 93.2 (2009), pp. 176 –182.

[21]   J. van de Groep and A. Polman. "Designing dielectric resonators on substrates: Combining magnetic and electric resonances". In: *Opt. Express* 21.22 (2013), pp. 26285–26302.

[22]   Jorik van de Groep. "Resonant Nanophotonic Structures for Photovoltaics". PhD thesis. University of Amsterdam, Dec. 2015.

[23]   Seungkyu Ha et al. "Tunable top-down fabrication and functional surface coating of single-crystal titanium dioxide nanostructures and nanoparticles †". In: *Nanoscale* 8 (2016), p. 10739.

[24]   Ion Michael Hancun. "Controlling the Multipolar Interference of Nanoantennas". PhD thesis. 2019.

[25]   J. Hansen et al. "Ice melt, sea level rise and superstorms: evidence from paleoclimate data, climate modeling, and modern observations that 2 C global warming could be dangerous". In: *Atmospheric Chemistry and Physics* 16.6 (2016), pp. 3761–3812.

[26]   Chen Hu et al. "The micropatterning of layers of colloidal quantum dots with inorganic ligands using selective wet etching". In: (2014).

[27]   Rachelle Ihly et al. "The photothermal stability of PbS quantum dot solids". In: *ACS Nano* (2011).

[28]   N. Lenssen et al. "Improvements in the GISTEMP uncertainty model". In: *J. Geophys. Res. Atmos.* 124.12 (2019), pp. 6307–6326.

[29]   Francesco Meinardi et al. "Highly efficient large-area colourless luminescent solar concentrators using heavy-metal-free colloidal quantum dots". In: *Nature Nanotechnology* 10 (2010), 878 EP –.

[30] Francesco Meinardi et al. "Highly efficient luminescent solar concentrators based on earth-abundant indirect-bandgap silicon quantum dots". In: *Nature Photonics* 11 (2017), 177 EP –.

[31] Gustav Mie. "Beiträge zur Optik trüber Medien, speziell kolloidaler Metallösungen". In: *Annalen der Physik* 330.3 (1908), pp. 377–445.

[32] Andrey E. Miroshnichenko et al. "Nonradiating anapole modes in dielectric nanoparticles". In: *Nature Communications* 6 (Aug. 2015), 8069 EP –.

[33] Kyra Orbons. "A Survey of Contemporary Research in LSCs". In: (July 2018).

[34] J.C. Pales and C.D. Keeling. "The concentration of atmospheric carbon dioxide in Hawaii". In: *Journal of Geophysical Research* 70 (1965), pp. 6053–6076.

[35] Yuriy A. Artemyev Alina Karabchevsky Alexander S. Shalin Andrey B. Evlyukhin Pavel D. Terekhov Kseniia V. Baryshnikova. "Optical multipole resonances of non-spherical silicon nanoparticles and the influence of illumination direction". In: 10528 (2018).

[36] David Spratt. *CLIMATE REALITY CHECK. After Paris, counting the cost.* May 1, 2016. URL: https://docs.wixstatic.com/ugd/148cb0_9c80333f46ec4da8a2e8d7ba41886df6.pdf (visited on 07/25/2019).

[37] Isabelle Staude, Thomas Pertsch, and Yuri Kivshar. *All-dielectric resonant metaoptics goes active*. Tech. rep.

[38] Isabelle Staude et al. "Tailoring Directional Scattering through Magnetic and Electric Resonances in Subwavelength Silicon Nanodisks". In: *ACS Nano* 7.9 (2013). PMID: 23952969, pp. 7824–7832.

[39] *The Keeling Curve 1700–present*. July 27, 2019. URL: https://scripps.ucsd.edu/programs/keelingcurve/ (visited on 07/27/2019).

[40] Climate Action Tracker. June 2019. URL: https://climateactiontracker.org/countries/ (visited on 07/26/2019).

[41] Yera Ye Ussembayev, Zeger Hens, and Kristiaan Neyts. "Contrasting Anisotropy of Light Absorption and Emission by Semiconductor Nanoparticles ACS Photonics XXXX, XXX, XXXXXX". In: 14 (2019), p. 43.

[42] Kaifeng Wu, Hongbo Li, and Victor I. Klimov. "Tandem luminescent solar concentrators based on engineered quantum dots". In: *Nature Photonics* 12.2 (2018), pp. 105–110.

[43] Chenghui Xia. "Colloidal Copper Indium Sulfide-Based (Hetero)nanocrystals". PhD thesis. Utrecht University, 2019.

[44] Weiqiang Xie et al. "Integrated optics; (230.7370) Waveguides; (160.4236) Nanomaterials". In: *Opt. Express* 17.17 (2009), p. 4.

Acknowledgements

With the end of this project in sight, I am glad to acknowledge that this thesis could not have been completed without the people that supported me throughout the past year. First of all, thank you, Albert, for giving me the opportunity to extend my literature review with this project. It was inspiring to see how a small suggestion in a discussion was seized and turned into a serious project that has taken up most of my year. It was special (and at times challenging) to take the project to the drawing table and later into the lab, which you stimulated from the start.

Tom supervised me throughout the project and will hopefully bring it to a higher level after my departure. Thank you for showing me around at AMOLF and for helping me further throughout the project, especially when I felt discouraged by the slow progress of the research.

Katerina, thank you for taking the time to attend my final presentation and for reading and grading this thesis.

Nick, it was great to share the office with you. I enjoyed your physics-enthusiasm and I am very grateful for the time you took to help me out with theoretical struggles. Also, many thanks for the very last minute help with CL measurements, making me feel like a nearly full-fledged group member. Thanks to Stephan for helping me out with ellipsometry and quantum dot related issues. Best of luck in Australia! Magda, for the two-day scavenger hunt for pillars. Verena, for being a great supervisor for my literature research. And Matthias, please buy yourself a lunchbox, it will make life more pleasurable. To the group as a whole, also those I didn't specifically mention. And Matthias, please buy yourself a lunchbox, it will make life more pleasurable.

I would also like to thank Chenghui Xia and Tim Prins for providing me with the quantum dots without which this project would not have been possible. Chenghui also for answering so many of the questions that I had, and Tim for answering even more and showing me around in a different lab. Also, thanks to Bob and Dimitry, for the training, the fun, and helping out with fabrication strategies.

Finally, and most of all, I would like to thank the people outside of AMOLF who helped me keep going, endured my frustrations and made sure there was plenty of enjoyment in the hours that were not dedicated to my research. Weiyi, for introducing me to running, which kept me sane over the winter. Steven, for a different perspective on life and taking me to ceramics, which gave me so much joy in spring. And, of course, Loe, for your endless patience, encouragement, the laughs, the revisions, and for always making sure that I don't miss out (too much) on food and sleep.